Engineering Failure Analysis 158 (2024) 107984

Contents lists available at ScienceDirect

Engineering Failure Analysis

journal homepage: www.elsevier.com/locate/engfailanal

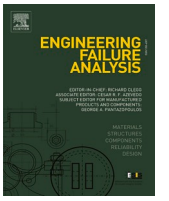

Photogrammetry-aided numerical seismic assessment of historical structures composed of adobe, stone and brick masonry. Application to the San Juan Bautista Church built on the Inca temple of Huaytará, Peru

Emerson Cuadros-Rojas [a], Savvas Saloustros [b], Nicola Tarque [c,d], Luca Pelà [a,*]

[a] Department of Civil and Environmental Engineering, Universitat Politècnica de Catalunya (UPC-BarcelonaTech), Jordi Girona 1-3, 08034 Barcelona, Spain
[b] Laboratory of Earthquake Engineering and Structural Dynamics (EESD), École Polytechnique Fédérale de Lausanne (EPFL), GC B2 495, Station 18, 1015 Lausanne, Switzerland
[c] Department of Continuum Mechanics and Structures – E.T.S.I Caminos, Canales y Puertos, Universidad Politécnica de Madrid, C. Prof. Aranguren 3, 28040 Madrid, Spain
[d] Gerdis Research Group, Civil Engineering Division, Pontificia Universidad Católica del Perú (PUCP), Av. Universitaria 1801, Lima, Peru

ARTICLE INFO

Keywords:
Adobe
Masonry
Dry-joint carved stone
Structure-from-motion photogrammetry
Earthquake
Pushover analysis
Inca structure

ABSTRACT

This research presents a cost-effective surveying methodology to assist the seismic assessment of complex heritage buildings, based on terrestrial structure-from-motion (SfM) photogrammetry. The method was applied to the study of the seismic performance of the church of San Juan Bautista – Inca temple of Huaytará, Peru, an emblematic case study due to its complex architecture and coexistence of different construction materials. The geometrical model for the seismic assessment was developed with an error of less than 2 % using SfM photogrammetry. Non-linear static pushover analyses were performed on 3D FEM models of the nave and the towers to evaluate their individual response under seismic loading. Mechanical properties of different structural materials of the church were evaluated based on laboratory experimental tests on mortar and adobe, contemporary and ancient fired brick, Inca stone, colonial stone and rubble stone units. Non-linear pushover analyses were conducted in four directions perpendicular to the perimeter walls, and the response of the structure was compared with the seismic demand specified in Peruvian Standards. The simulations show that damage-prone areas are the western and eastern facades, with cracking at the connections between orthogonal walls, as well as at the interface of adobe masonry with Inca stone masonry. The towers exhibit similar seismic response, with lower strength capacities compared to the main nave. In this case, flexural overturning mechanisms and cracking at the interface between stone and adobe masonry were observed. The displacement-based seismic assessment using the N2 method shows that a peak ground acceleration of 0.21 g could lead to the collapse of the north and south facades of the main nave. The towers showed a much smaller capacity with PGA leading to collapse of approximately 0.09 g. Overall, this study contributes to the understanding of the seismic performance of the Huaytará-Huancavelica church, highlighting vulnerabilities and providing valuable information for its preservation and future interventions. Future investigations should focus on on-site tests that will

* Corresponding author.
E-mail addresses: emerson.julio.cuadros@upc.edu (E. Cuadros-Rojas), savvas.saloustros@epfl.ch (S. Saloustros), nicola.tarque@upm.es (N. Tarque), luca.pela@upc.edu (L. Pelà).

https://doi.org/10.1016/j.engfailanal.2024.107984
Received 5 December 2023; Received in revised form 11 January 2024; Accepted 14 January 2024
Available online 20 January 2024

allow the estimation of the effect of existing damage on the structural response and their incorporation in the numerical model.

1. Introduction

Sun-dried earth construction is widespread throughout the world, like in the Middle East, Western Asia, North Africa, West Africa, South and North America, as well as in Europe [1–3]. Adobe masonry, in particular, is one of the primary traditional construction materials and one of the most recurrent building techniques in numerous countries [1,2]. The widespread use of adobe masonry is due to the low cost and large availability of the required resources for its construction. Indigenous peoples of the Americas had primarily employed adobe for several thousand years, as in Añancusi. Even though the Spanish Conquistadors introduced the use of fired clay bricks, adobe construction remained the main building material for centuries in many countries of South America, and it is still widely used in vernacular construction in rural areas.

Adobe structures are vulnerable to different types of actions due to their limited strength and brittleness, and especially to seismic actions, as recently recorded after the earthquakes occurred in El Salvador (2001), Iran (2003), Peru (1970, 1996, 2001, 2007, and 2021), Mexico (1932, 1941, 1973, 1985, 1995, 2003 and 2017) [4–6], Ecuador (1856, 1906, 1979, 1987, 1998, 2010, 2014, 2016, and 2022) [7], Chile (1835, 1868, 1877, 1906, 1939, 1922, 1943, 1949, 1960, 1985, 1995, 2010, 2014, and 2015) [8], Pakistan (2005), and China (2008 y 2009) [9]. The lack of box behaviour in these structures, due to the poor wall-to-wall connection combined with the common presence of a flexible diaphragm, results in separation of orthogonal walls and their out-of-plane failure. For in-plane actions, the poor mechanical strength of adobe results in in-plane damage in the form of diagonal shear cracking or flexural cracking for high or low axial load ratios, respectively.

There are numerous studies and databases [9–11] about the mechanical behaviour of adobe, with different characterisation results according to the country of origin, e.g. Cyprus [11], Iran [12], France [13], Portugal [14], Italy [15,16], Morocco [17], China [18,19], Mexico [20], Colombia [21–23], and Peru [24,25]. These studies indicate a compressive strength of adobe ranging between 0.29 and 3.2 MPa. Besides seismic actions, other hazards are those related to settlements, wind loading, water erosion, and damp, among others.

Adobe in many countries is often combined with other traditional building materials, resulting in a wide range of mixed structural forms. Some emblematic examples are the adobe-timber mixed structures in Peru and Chile [26–28], as well as the adobe-stone mixed structures existing in Peru that constitute the meeting point of Inca and Spanish Colonial architectures. Current research still requires the development of novel methods for inspecting and analysing this type of structures, according to the modern approaches for conserving historical buildings [29,30].

The analysis of historical structures usually requires the preparation of computer-aided 3D geometric models (CAD) due to the complex geometry and coexistence of different members with elaborated shapes and morphology. This activity is preliminary to build numerical models, like those based on the Finite Element Method (FEM), applicable to execute the structural assessment and decide the possible need of complementary studies or ad-hoc interventions for preservation. Architectural survey based on topography is a rather popular technique, as well as other emerging ones like laser scanning and photogrammetry, either terrestrial or supported by unmanned aerial vehicles [31–41]. Most of these techniques allow the generation of a point cloud that is helpful to build a 3D geometrical model as input for the FEM software. Different semi-automatic [42–46] and, recently, automated approaches for the generation of 3D geometrical models [47] or FE models [48] of regular geometries have been proposed in the literature.

Building a reliable FEM model of a historical structure is still very challenging nowadays, as the analyst often has to make hypotheses to simplify the complexity of the model, correctly represent the distribution of the composing construction materials, and accurately describe their mechanical behaviour. These aspects are even more challenging to address in unique heritage buildings, which result from several construction stages during their history, have experienced damage and degradation, and have diverse coexisting architectural styles, structural members, and construction materials. The realistic elaboration of a numerical model of a historical structure should include evidence from physical in-situ or laboratory experimental tests (e.g. [49–53]) and calibrated such that numerical results correlate well with existing damage and/or deformation (e.g. [34,47–51,54,55]. In this way, calibrated numerical models can be useful for identifying the main structural weaknesses, quantifying structural capacity, and subsequently aiding to a data-drivel retrofit strategy [52,53,56].

This research contributes to the abovementioned issues by presenting a cost-effective methodology to support the numerical seismic assessment of historical complex adobe and masonry structures. The proposed methodology is based on the generation of the numerical model through images and structure-from-motion photogrammetry. The method was applied to the study of the church of San Juan Bautista – Inca temple of Huaytará, Peru, as it constitutes a unique case due to its complex architecture and coexistence of different materials (dry-joint stone masonry, adobe, stone and brick masonry), which is the result of a long construction period dating from the Inca period up to modern times. After presenting the photogrammetric surveying approach, the paper presents a study of the selected historical complex, including all the necessary complementary activities required in modern conservation, ranging from the historical survey, the in-situ fieldwork, the experimental laboratory tests, and the non-linear structural analysis based on the use of a FEM model. The experimental tests are an important reference for the mechanical properties of clay and adobe bricks, as well as Inca stone elements used in similar structures of the region. Seismic assessment was performed through non-linear static analyses with mass-proportional earthquake-equivalent loading pattern, providing results in terms of observed damage in agreement with the current condition and past structural performance. The research gives insights on the current state of conservation of the structure and the causes of the observed damage (especially those due to Pisco earthquake in 2007), which could constitute the base for future

preservation studies of this important heritage construction site.

2. Photogrammetric survey

One of the intrinsic characteristics of ancient heritage structures is the complex geometry, which is a result of the architectural design and the multiple structural alterations that occurred during the history, as well as of the damage (both environmental and anthropogenic). The digitalisation of complex geometry often requires important resources, expensive equipment, and time-inense fieldwork and desk post-processing of acquired data. All these constitute currently important limitations for the managers of the historical sites.

Structure-from-Motion (SfM) Photogrammetry [57] is currently a low-cost alternative to more traditional surveying techniques. The efficiency and accuracy of SfM has been validated by LIDAR techniques and Terrestrial Laser Scanner (TLS) [58]. Works using photogrammetry are available in the field of geosciences [58–62], and more recently in the field of the analysis of historical buildings [39,40,62,63].

This paper presents a low-cost application of SfM photogrammetric surveying on a highly complex case study, showing to be cost-effective, versatile and applicable to other types of heritage structures. Fig. 1 shows the flowchart summarising the main steps of the used workflow, which are also described in the following.

- Preliminary desk survey to gather all the existing historical information, e.g. documents, photographs, and plans. If available, geographic maps and satellite images can also contribute to defining a first remote approach to the location of structure. This is important for identifying the on-site route for image-acquisition and any possible limitations.
- Analysis and interpretation of climatic summary data in light of probable impacts on fieldwork operations. Preliminary careful assessment of weather and light conditions during the days planned for the photogrammetry plays a crucial role since the possible presence of shadow or bad weather conditions (e.g. rain, snow) can jeopardise the quality of the SfM photos [60,64].
- Regarding the schedule of photo-taking operations, it is advisable to consider different times of the day to correct shadows, reflections, and excessive brightness that might appear on other portions of the structure, as all these aspects may jeopardise the quality of the SfM model [60]. According to the authors' experience, taking pictures on different days with different light conditions is also advisable to improve the photogrammetric model's quality.
- Study the routes for image-taking operations according to the site's morphology, access, topography and the presence of neighbouring properties. The routes for photo taking should be parallel to the facades of the building, as shown in Fig. 2 [65], but if this is not possible it is convenient to increase the number of photographs from different angles, i.e. the so-called 'tie pictures' [39,40]. In terrestrial photogrammetry, the access to hidden parts of the buildings, such as roofs and towers, might be adequately addressed by photo taking from neighbouring buildings or hills and using platforms.
- Choose the camera parameters. Higher resolution results in higher quality reconstructions, but also to a larger amount of data (images and processed files). The choice of the camera resolution depends therefore on the desired accuracy [66].

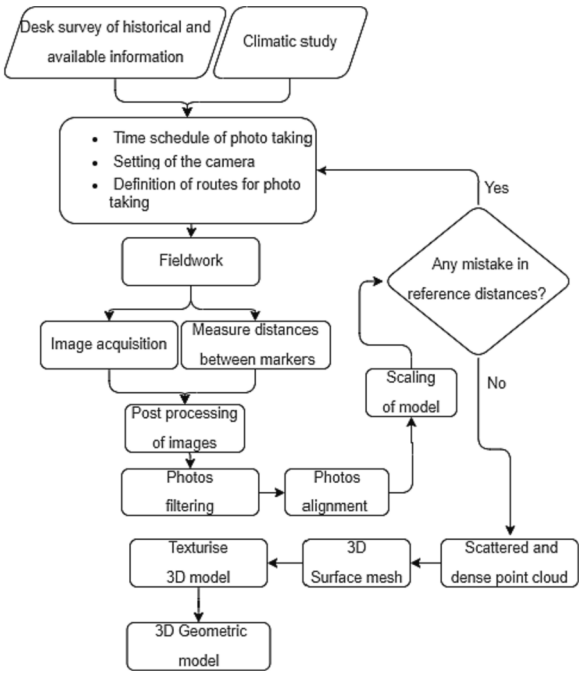

Fig. 1. Flowchart of the workflow for the proposed methodology of photogrammetric surveying.

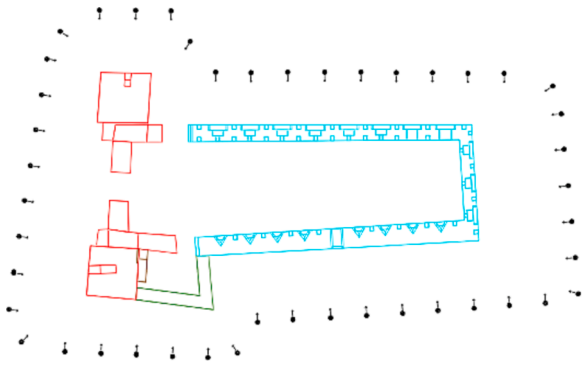

Fig. 2. Example of routes for photo taking parallel to the perimeter of the building.

- On-site photo-taking should produce at least double overlapping pictures to generate the necessary overlapped points to build the point cloud.
- During the field work, it is advisable to place markers easily accessible from different positions (e.g. corners between main and lateral façades) so that many photos can capture them. The distances between the markers must be measured precisely on-site to provide reference lengths to scale the 3D model.
- Post-processing using software can keep control of all the different steps of the digitalisation of the 3D model to edit possible defects. Several open-access algorithms and software are available for all the different levels of the digitalisation of the model [66–69].
- Filtering of the photos according to their quality.
- Alignment of the photos using markers. This operation consists of identifying common points in pictures sharing an overlap. Alignment allows deriving the geometric coordinates of the photo capture position. Common points in overlapping photographs can be on corners, edges of towers, basement walls, corners of doors and windows, etc.
- Scaling of the model by inserting the distances between markers previously measured on site, i.e. the so-called scale bars.
- Building the scattered point cloud calculated from the positions of the photos' capture after filtering pictures with a limited number of scattered points.
- Building the dense point cloud through the interpolation of the encountered scattered points. All the points that do not pertain to the surveyed object have to be deleted, e.g. those referring to neighbouring trees, buildings, vehicles, people, etc.
- Generation of the 3D mesh surface starts from the vector generation of the dense point cloud. This information can be exported to a CAD software to edit the model, delete mistakes and generate the 3D geometric model.
- Texturization of the 3D model using scaling and overlapping of figures up to the final execution of the 3D photogrammetric model.

3. Case study: Church of San Juan Bautista – Inca temple of Huaytará, Peru

3.1. Historical survey

The historical complex of the church of San Juan Bautista – Inca temple of Huaytará (Fig. 3), located in the department of Huancavelica, Peru, has been a witness of all times in Peruvian history. Due to its strategic location on the road of penetration to the Peruvian Andes, *Ushkush Inkañan*, it was visited by Chankas, Incas, Conquistadors, independentists, republicans, invaders, and fighters of the internal armed conflict.

The construction of the temple started around of 1470 D.C [70,71] under *Astohuarakata* by order of the Inca *Pachacutec* as a structure that allowed expanding the influence of the nascent Inca empire on rebel populations [72]. The structure of the Inca temple

Fig. 3. a) Exterior, b) interior views of the church of San Juan Bautista – Inca temple of Huaytará, and c) drawing by Max Uhle in 1902[73].

remained intact until the church's construction over it at the time of the Viceroyalty of XVI century [71]. Since then, the building has undergone multiple alterations that make it a unique heritage site in Peru, as its structure includes practically all the most important traditional construction materials of Latin America, e.g. carved stone with dry joint, adobe, brick, mud mortar, and timber. It is possible to identify five different construction stages over more than six centuries (XV – XXI), related to five important historical periods in Peru (see Fig. 4).

1) Construction of the Inca temple in the XV century [70,71]. Composed of dry-joint carved stones, the Inca temple had a trapezoidal shape, with the east wall longer than the west wall. A triangular Inca adobe wall still exists over the west stone wall, which had the function of supporting the original Inca gable roof made of logs and *Ichu* [74], see Fig. 5a. The temple had two entries on the south wall, one entry on the north wall, and most probably one on the east wall as typical in Inca architecture.
2) Construction of the Colonial church in the XVI century [71]. The church's construction over the ancient Inca temple required the demolition of the east wall, which probably resembled the west wall composed of a lower stone and an adobe upper triangular part. The removed stones from the demolished east wall and mud mortar served as basements of the extensions of the north and south adobe walls and for constructing the towers' foundation [72]. Adobe walls were built on top of the existing Inca walls [71] along the north and south façades up to 7.70 m, including three windows to provide more light to the interior. The height of the Inca triangular adobe wall on the west side was raised with a new adobe addition to increase the size of the nave up to 11.00 m. The new main façade was built on the east side, as well as the lower part of the two towers, including the basement made of rock and mud, the adobe walls, and the interior corridors, and the upper part of the south tower composed of four squat columns roofed by tiles, see Fig. 5b.
3) Additions during the Republican period (early XX century). This construction stage corresponds to the completion of the north tower (1925, [75]), including the upper hollow columns and the dome, everything made of clay brick masonry of the time. This new addition was employed to host the belfry that was moved from the dismantled south tower, see Fig. 5c.
4) Additions during the late XX century. This period refers to the construction of the sacristy behind the north tower in the 1980s. The upper part of the south tower was constructed with brick units and cement mortar in the 1990s, see Fig. 5d. A reinforced concrete slab was placed on the base of the four hollow masonry columns and the masonry block that supports the dome. The dome has arched windows on all four sides. The total height of this tower, including the dome, is 16.75 m.
5) Recent additions during the XXI century. The dome of the north tower was demolished by the 2007 Pisco earthquake (Mw 8.0), see Fig. 5e, and its reconstruction was completed in 2009 by maintaining the original shape. The total height of the north tower is currently 16.75 m, see Fig. 5f.

The historical survey provided valuable information about the construction of the heritage site and events that left evidence on the structure. Besides the 2007 Pisco earthquake already mentioned, according to the chronicles available [76], another earthquake of Modified Mercalli intensity VIII occurred in 1470, which coincided with the initial construction stage of the Inca temple. Therefore, the possible damage could have been repaired at that time. In addition, the church suffered three major fires, in 1914, 1938, and 1984 [72]. The 1938 fire was the most disastrous and consumed the wood panelling of the interior walls. The evidence of this fire on the stone walls can still be seen today from the interior. More information on the historical survey can be found in [77].

3.2. Construction materials

According to the historical survey and the in-situ inspection, eight different types of construction materials were identified, corresponding to the various construction periods, see Fig. 6 and Fig. 7.

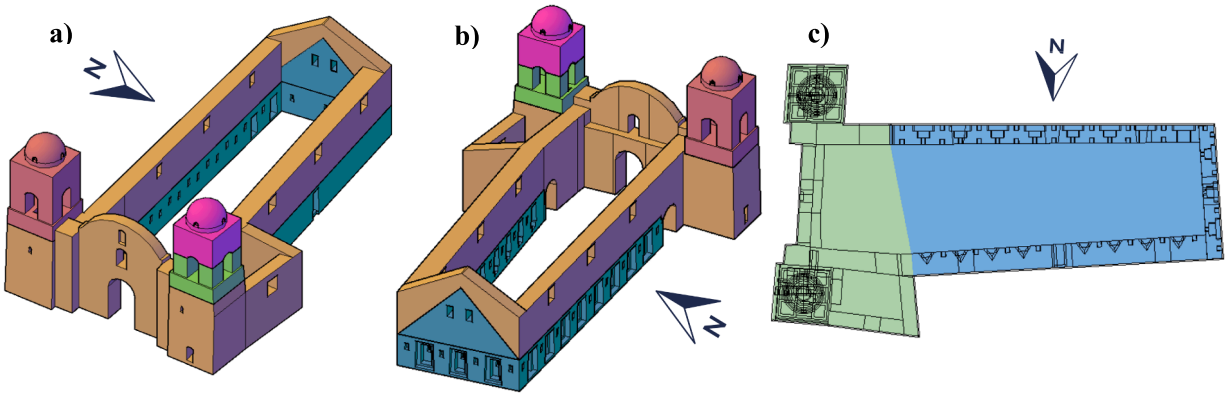

Fig. 4. Parts of the structure according to construction period: light blue denotes the Inca period, brown the Viceregal period, green the Republican period, red the late XX century, and pink the XXI century (colours visible in the electronic version of the manuscript, a) south-east, b) north-west, and c) plan views. (For interpretation of the references to colour in this figure legend, the reader is referred to the web version of this article.)

Fig. 5. a) Reconstruction of the original Inca temple, b) photo by Max Uhle in 1902, c) photo by Luis E. Valcárcel in 1940, d) photo by Mario Ibáñez during the reconstruction of the south tower in 1990, e) north tower damaged by 2007 Pisco earthquake, and f) current appearance of the church in 2019.

1) Inca carved stone masonry with dry joints. The edges of carved stones have recesses highlighting the joints with other rocks. No texture or type of rock differences have been found throughout the structure. The quarry where the stones come from is 25 km above the mountains adjacent to the archaeological centre of Inca-Huasi. The stone blocks are larger for those located at higher heights. The vertical joints are cut for each course, giving more consistency to the wall. The windows' lintels and jambs are made of a single piece of rock.
2) Viceroyalty stone masonry. This masonry is part of the foundation of the Viceregal structures, such as the later extensions of the original lateral north and south walls, and the façade. It is formed by an arrangement of rocks with mud, almost orderly. The stone units came from the Inca wall of the east side that was dismantled during the Viceroyalty.
3) Adobe masonry. There are two types of adobe, one dating from the Inca period, which forms the triangular part of the west wall, and the other from the Viceroyalty period, which includes the third upper part of the west, north and south walls. The units are approximately $0.50 \times 0.30 \times 0.15$ m^3 and joined with 10 to 20 mm thick mud mortar.
4) Old brick masonry. This material is located in the second part of the north tower in elevation, identified with the green colour in Fig. 6. It is characterised as masonry made of handmade fired clay brick units of $0.25 \times 0.13 \times 0.05$ m^3 and lime mortar, and these materials date from the 1930 s.

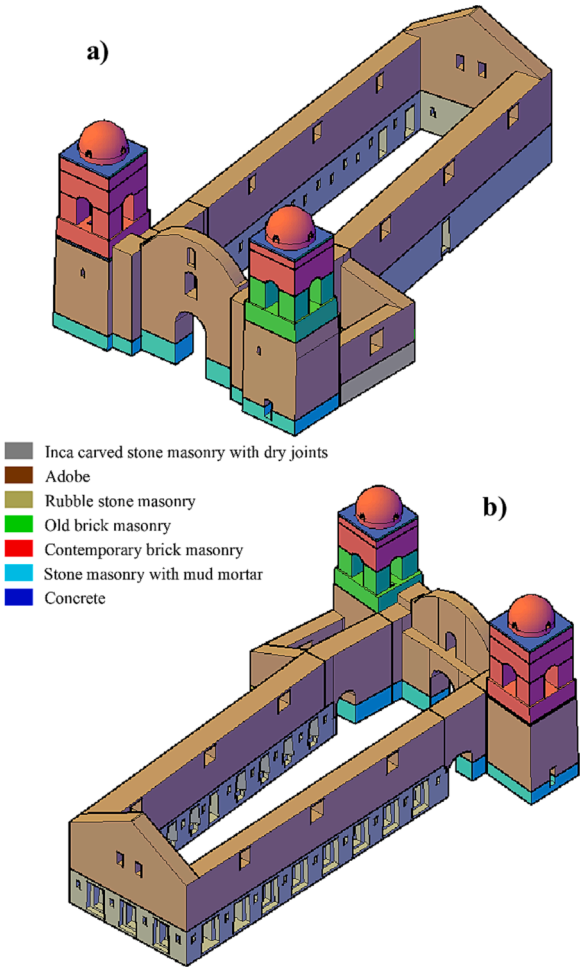

Fig. 6. Construction materials of the church of San Juan Bautista (colours visible in the electronic version of the manuscript). a) south-east, and b) north-west views.

5) Contemporary brick masonry. This material covers the two reconstructions carried out in the 1990 s and 2009 in both towers, and it is made up of handmade fired clay brick units of $0.21 \times 0.12 \times 0.086$ m^3. The mortar is made of cement and sand, and the thickness of joints varies between 5 and 20 mm.
6) Rubble stone masonry. This masonry is the foundation of the current sacristy, and it is composed of stones of different sizes and shapes according to an irregular arrangement. The stone units do not come from the Inca wall; they are joined with earth mortar of variable thickness.
7) Concrete. Material used to construct the slabs in the 1990 s by local craft in both the north and south towers.
8) Timber. The gable roof of the church is made up of timber trusses, on which there are zinc-aluminium sheets (*calaminas*), which only rest on the adobe side walls.

3.3. Damage survey

After centuries and almost no conservation, the structure's damage is evident nowadays. The Inca walls evidence stone separations, the presence of vegetation in between the blocks, especially in the lower courses, and section loss due to erosion and previous fires. The adobe walls of the nave (north and south) present cracks and loss of integrity due to humidity. The north tower shows important cracks in its interior, especially near the corridor. Both towers also exhibit horizontal cracks in the boundary zone between stone and adobe masonry. There is damage due to rainwater erosion at the edge between the south wall and the south tower. At the top of the towers made of brick masonry, there are problems of efflorescence and loss of mortar section, and moisture damage at the base of the columns and the dome. Fig. 8 shows a graphic summary of the damage reported during the field visit.

Fig. 7. Construction materials: a) Inca carved stone masonry with dry joints in the south and b) north walls, c) viceroyalty stone masonry at the base of the towers, d) adobe in the south wall, e) old masonry in the north tower, f) contemporary masonry in the south tower, g) rubble masonry in the basement of the sacristy, h) concrete slab in the south tower, and i) view of the timber roof.

4. Construction of the 3D geometric model through photogrammetry

4.1. Photogrammetric survey

The methodology presented in Section 2 was applied to the church of San Juan Bautista – Inca temple of Huaytará, Peru, to obtain the 3D geometric model. The following steps were considered during the research and more information is available in [77].

- Analysis of the historical information, whose outcome has already been presented in Section 3.1. Available drawings were executed in the past by Max Uhle in 1902 [72] (Fig. 3-c), and by Graziano Gasparini in 1977 [73]. In addition, some plans were available in the archives of the Ministry of Culture and Province of Huaytará.
- The climatic study was obtained for the site, which is located in the Peruvian Andes at 2,720 m height, and also derived from the closest meteorological station *Estación Tambo* about the SENAMHI (*Servicio Nacional de Meteorología e Hidrología del Perú*), with historical temperatures ranging from −4°C and 21.2 °C.
- The schedule was established for different days and times, both in the morning and afternoon, to capture photos with other light conditions according to the meteorological conditions.
- The routes for photo taking were established around the perimeter of the construction, as shown in Fig. 2. Surrounding hills allowed photo taking also from convenient positions to capture tall objects, e.g. the roof and the bell towers.
- The camera settings considered 6,000 × 4,000 pixels and 18 mm focal length. The camera was handheld without a tripod.

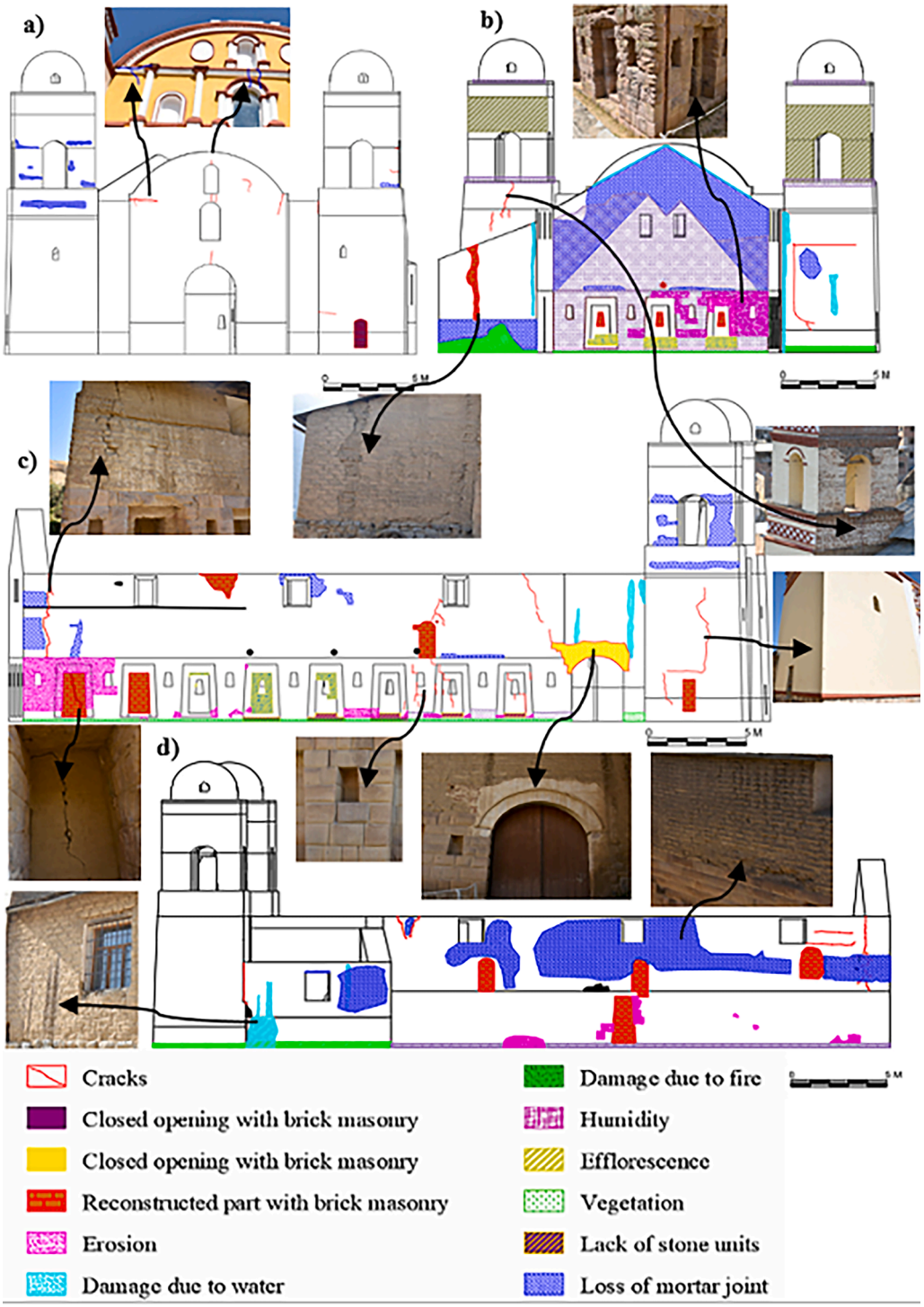

Fig. 8. Damage survey: a) East, b) west, c) north, and d) south façades.

- During the fieldwork, the photos were taken from many positions, see Fig. 9a, on different days trying to achieve the same lighting conditions for all sides of the structure. References distances between markers were measured by using a laser distance meter, allowing the creation of scale bars in the photogrammetric model, see Fig. 9j. Markers were redundant (Fig. 9b) and placed in strategic points within the overlaps among different photos, e.g. in corners of façades, doors, windows, etc.
- The software Agisoft Metashape [65] was used to post-process the photos, after appropriately filtering the images to select the highest quality.

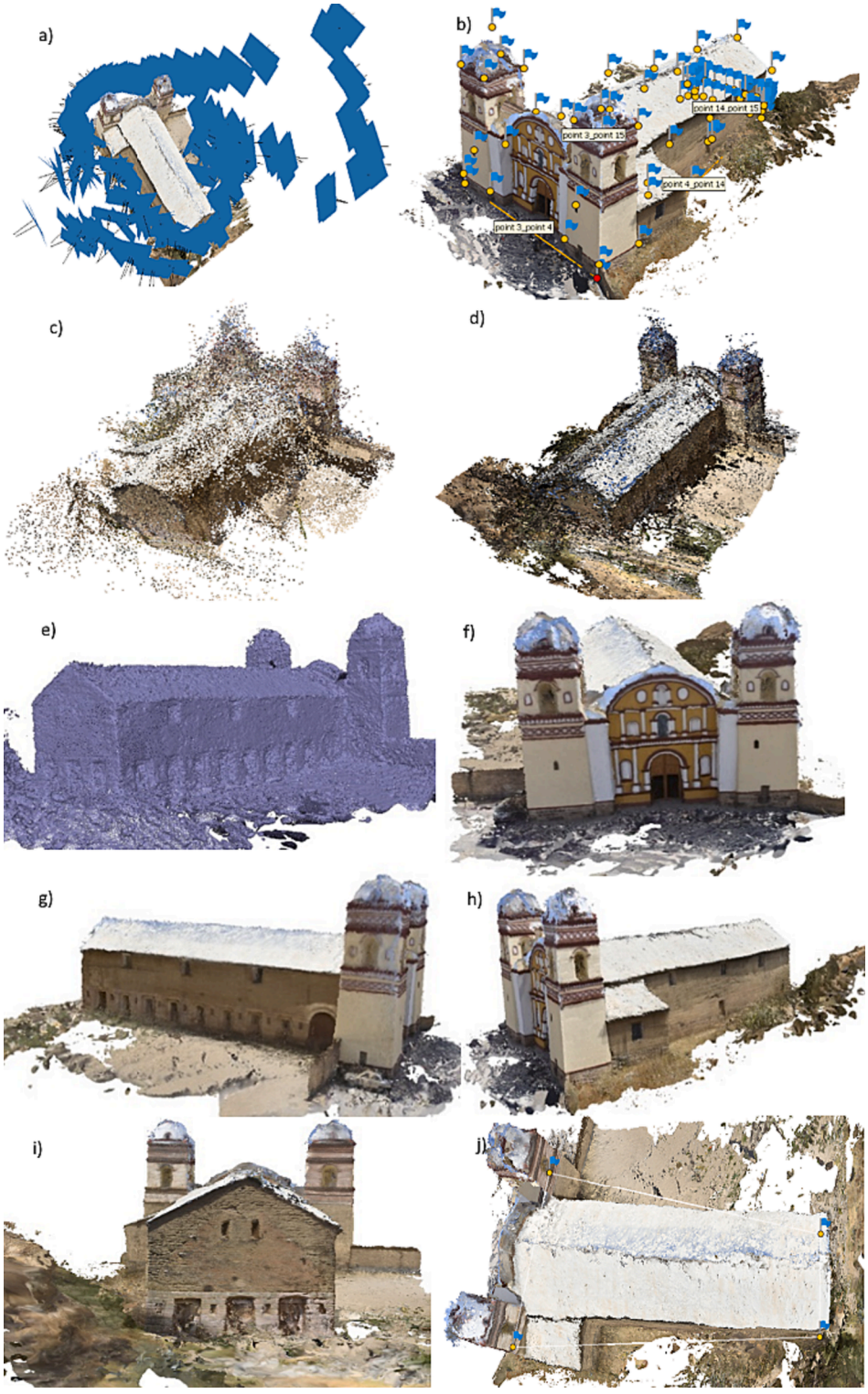

Fig. 9. Construction of the photogrammetric model of the church of San Juan Bautista – Inca temple of Huaytará: a) positions of captures of photos, b) control points for the calibration of the photogrammetric model, c) scattered point cloud, d) dense point cloud, e) 3D surface mesh, f) front, g) south, h) north-east, i) west, and j) plan views of the textured model.

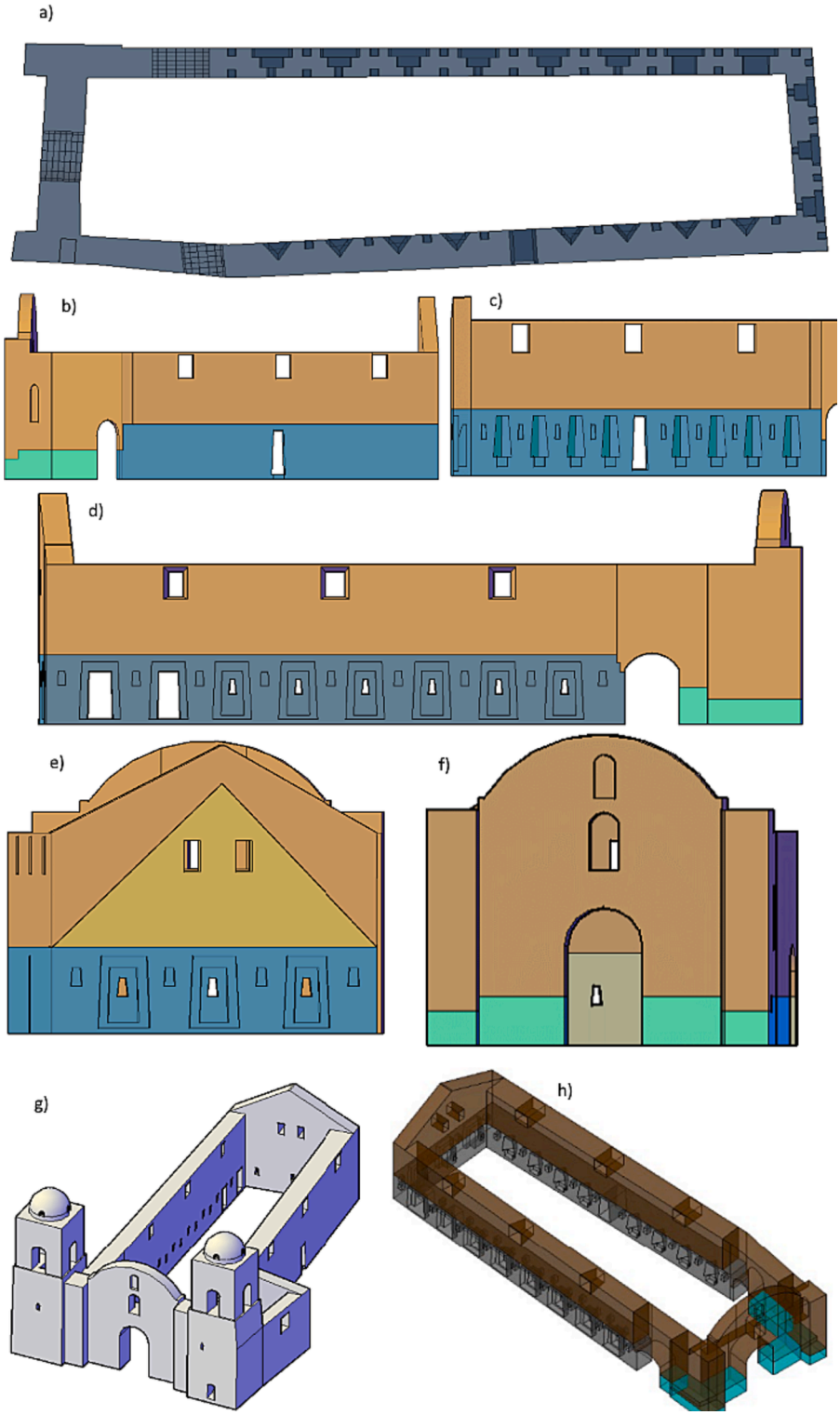

Fig. 10. Legend of the views of the 3D geometric model: a) Plan view of the constructed model, b) north exterior view, c) north interior view, d) south exterior view, e) west exterior view, f) east exterior view, g) north-east perspective of the 3D model, h) south-east perspective of the 3D model with translucent effect.

- The alignment and scale of the model were executed according to the scale bars established previously.
- Mistakes in reference distances were checked after using a 2 % threshold, according to previous studies [63], to verify the coherence between the reference distances measured on-site and the relevant ones in the photogrammetric model, see Fig. 9j.
- A 3D scattered point cloud was obtained based on photo alignment, see Fig. 9c. The points outside the investigated object were deleted, e.g. those on neighbouring buildings, trees, vehicles, people, clouds, etc. The 3D dense point cloud was then obtained (Fig. 9d) to be exported as a 3D surface mesh (Fig. 9e), allowing the recognition of the morphology of structural members and architectural elements (Fig. 9e).
- The photogrammetric model was exported to a CAD 3D environment to create the 3D geometric model.
- The 3D model was finally texturised applying the photos taken. Figures Fig. 9i show different views of the texturised model.

4.2. construction of the 3D geometric model

The 3D photogrammetric model was exported to a CAD environment for its improvement towards a 3D geometric model, including the necessary metric information for building the FEM model but discarding all the information not relevant from the structural point of view, such as architectural decorations, niches, statues, friezes, etc.

The construction of the 3D geometric model began with the base perimeter of the church, cutting the photogrammetric model at ground level. As mentioned in the previous section, checking the coherence between references distances in the model with those measured on site with a laser distance meter was paramount to guarantee the highest quality of the model. The model was oriented based on the geometric north derived from GPS reference points obtained on the building.

Due to the complexity of the church, the geometric model was built from the base to the roof, considering the changes in geometry of all structural members. All the layers were joined together to form 3D solids. Irregular elements such as the accesses to the towers (Fig. 11c) and the characteristic triangular niches required ad-hoc special site measurements due to their complex geometry in plan and height. Dimensions of interior structures and inner morphology of some parts were obtained from localised pits.

The 3D solids, which contain the metric information of the building, were grouped according to the different types of material (Fig. 10) to optimise the development of the FEM structural model. Finally, the 3D model was texturised to visually represent the construction (see Fig. 12).

The 3D CAD model of the church is composed of four parts, i.e. the nave (composed of north, east, south and west walls), the sacristy, the north tower, and the south tower.

The nave is almost rectangular, with a central entrance doorway. It is composed of the Inca stone walls, which practically form the base of the church and the upper additions of the Viceroyal adobe walls. The nave has six entrances, three of which are open and three are closed with adobe. The Inca structure presents three trapezoidal-shaped closed doors distributed along the north and south walls. Two other arch-shaped entrances are located north and south of Viceroyal adobe walls. The main entrance is located on the façade. There are two types of windows, i.e. Inca and Viceroyal. The windows from the Viceroyal period are 6.10 m above the floor, rectangular, with three located on the south wall and three on the north wall.

The east façade stands on a 1.20 m high rock and mud basement. This adobe wall is staggered, with a base thickness of 1.90 m until a height of 6.30 m, followed by a thickness of 1.12 m up to the top. The entrance is arched with a width of 2.80 m and a height of 5.00 m, above which there is an arched window and then an arched niche. At the top of the wall is a half-moon gable reaching a total height

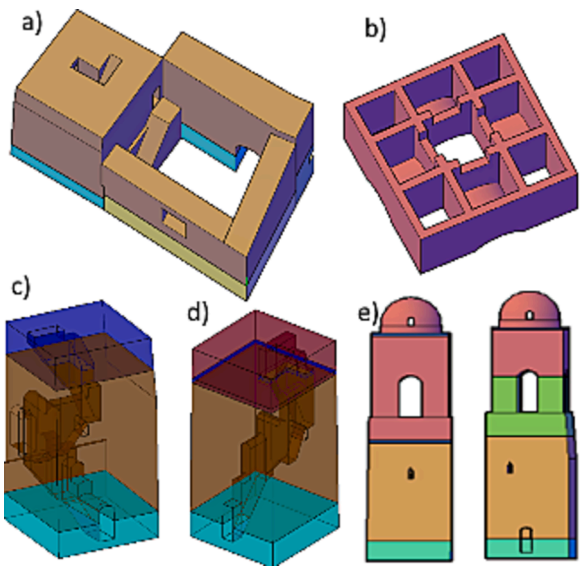

Fig. 11. Morphology and geometry of parts of the structure: a) sacristy and north tower, b) higher part of the north and south towers, c) interior of the north and d) south tower, and e) front view of both towers.

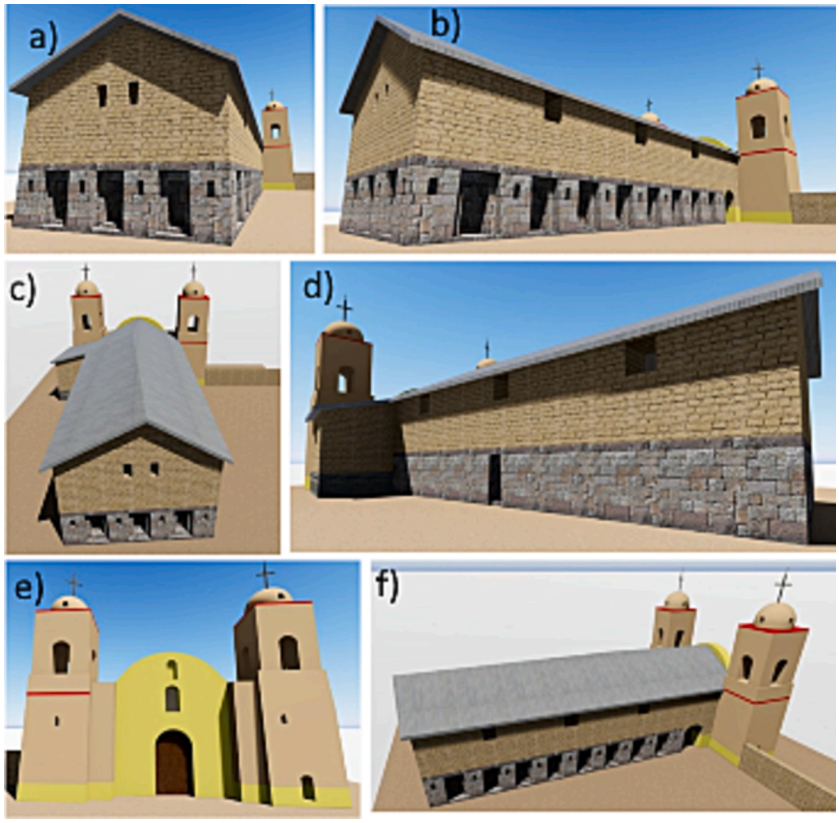

Fig. 12. Render of the church of San Juan Bautista – Inca temple of Huaytará derived from the 3D geometric model. a) West, b) southwest, c) west, d) north, e) east and f) west perspective views.

of 11.20 m. On the façade of this main entrance, there are several architectural elements, such as circular columns and reliefs of arch-like niches (Fig. 1 a).

The north wall comprises nine rows of dry-joint carved stone blocks from the Inca period and has an average height of 3.30 m and a length of 27.80 m. The wall has eight trapezoidal-shaped niches of 2.10 m height, with small trapezoidal-shaped near the top of the niches. Over the stone Inca wall, there is the 7.70 m high Viceroyal adobe wall. The adobe wall has three rectangular windows of 1.34 m in width. Below these windows, there are arched entrances sealed with adobe.

The church's south wall is also composed of the lower stone part, 27.82 m long and 3.30 m high, and of the upper Viceroyal adobe wall until the height of 7.70 m. The Inca wall presents two trapezoidal closed doors of 2×2.30 m^2 shape. Next, there are six double jamb niches with small windows, and at their sides, there are small trapezoidal niches, very similar to those on the north wall. The adobe masonry wall has three rectangular windows of 1.15 m width, 6.0 m above ground level, and an arched entrance of 2.65×3.40 m^2.

The west wall is composed of a stone wall and adobe masonry from the Inca period, and adobe masonry from the Viceregal period (Fig. 4). The wall is 11.45 m long and 11 m high, with the triangular gable on top. The Inca wall has three niches (closed) with double jambs of dimensions 1.80×2.75 m^2, with small trapezoidal niches at their sides. At the top of the Inca adobe wall are two small rectangular windows.

The sacristy, in the corner of the north wall and north tower, is made of an adobe wall founded on a rubble masonry basement of 1.75 m height. The entry is from the nave with an arched door and from the north tower through an adobe staircase of 1.0 m width. The external wall of the sacristy has one window of 1.35 m width at a height of 4.0 m from ground level. The sacristy has a single slope roof supported by the north wall at 7.0 m height and 6.30 m on the other side (Fig. 11a)

The north tower has a section of 4.80×4.90 m^2 and a total height of 16.75 m. It also has a trapezoidal entrance, currently closed. The south tower is square with a 4.95 m side. Regarding the access to the bell towers, there is an interior corridor with steps ranging from 0.6 m to 0.7 m wide and rising in a spiral shape. The entries to these corridors are trapezoidal and are located on the front side of the north tower and the side of the south tower. This corridor is connected to the exterior by small windows on the front side of the towers (Fig. 11). On top of the main body of each tower, there are four hollow columns of 1 m. Arches are joined at the top by 50 m side, 2.25 m height and 0.15 m thickness. These columns are covered by a 0.15 m thick reinforced concrete slab that forms the base for the upper portion supporting the semi-spherical domes. The columns sustain the upper part of the tower, with a 4.10 m side and 2.95 m height, with an interior core made of masonry allowing access to the domes, presenting four small windows in their lower part.

5. Experimental testing of the materials in the laboratory

Besides constructing the 3D geometrical model of the church, the careful evaluation of all the mechanical parameters is of paramount importance to feed correctly the FEM model of the building. For this reason, a comprehensive experimental program was carried out on extracted samples to assess the behaviour of the main historical construction materials. The experimental program took place in two laboratories, i.e. the Laboratory of Structures (LEDI) of the Pontifical Catholic University of Peru in Lima (PUCP) and the Laboratory of Technology of Structures and Materials (LATEM) at the Technical University of Catalonia in Barcelona (UPC-BarcelonaTech).

All the samples were extracted on site without affecting the integrity and cultural heritage, i.e. considering the original historical materials (pieces of Inca stones, old and contemporary units, etc.) available as remains inside the historical site. Due to the limited number of specimens available, the experimental program focused on the execution of compression tests on the materials, according to the European standard EN 772-1 [78] and the Peruvian standard E.070 [79] for bricks, the Peruvian standard E.080 [80] for adobe, the European standard EN 1926 [81], EN 14580 [82], the German standard DIN 18555-9 [83] for mortars, and the American Standard ASTM D 7012 [84] for stone.

5.1. Contemporary bricks

Five specimens of size approximatively 200 × 100 × 80 mm^3 were tested under compression at PUCP, see Fig. 13 a), d). The specimens were obtained from units collected on-site as remains of the reconstruction of the north tower in 2009. The loading rate was 100 kN/min, and the average compressive strength was 5.79 MPa (CV = 31 %) after applying the correction shape factor of 0.89 in compliance with the standard [78]. Table 1 presents a summary of the results for all the specimens tested.

5.2. Old bricks

Six specimens of size approximatively 100 × 100 × 50 mm^3 were tested under compression at PUCP, see Fig. 13 b), e). The specimens were obtained from units collected on-site as remains of the upper part of the north tower collapsed after the 2007 Pisco earthquake. The loading rate was 50 kN/min, and the average compressive strength was 8.53 MPa (CV = 31.8 %) after applying the correction shape factor of 0.75 in compliance with the standard [78]. Table 1 presents a summary of the results for all the specimens tested.

5.3. Adobe units

Six specimens of size approximatively 100 × 100 × 100 mm^3 were tested under compression at PUCP, see Fig. 13c), f). The specimens were obtained from units collected inside the historical site. The loading rate was 5 kN/min, and the average compressive strength was 0.56 MPa (CV = 8.8 %). Table 1 presents a summary of the results for all the specimens tested.

5.4. Stone

Nine specimens were tested at PUCP, and thirteen samples were tested at UPC, with a diameter of approximately 55 mm for both series of samples, with a height of around 115 mm for the first series and of 55 mm for the second series, see Fig. 14. The specimens

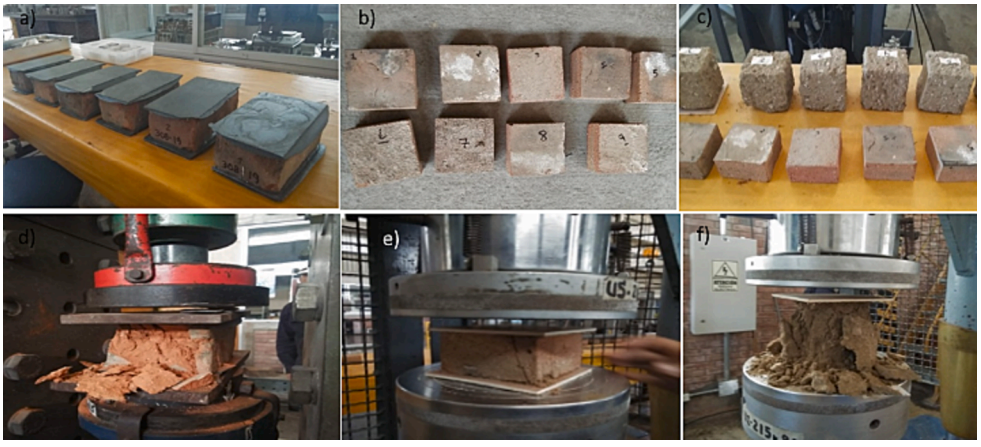

Fig. 13. Compression tests on various masonry units carried out at PUCP laboratory, a) Preparation of whole units of contemporary bricks, b) 100 mm × 100 mm specimens of old bricks, c) 100 mm cubic specimens of adobe bricks and specimens of old bricks, d) Compression test of contemporary bricks, e) Compression test of old bricks, and f) Compression test of adobe bricks.

Table 1
Summary of compression tests results from old bricks, contemporary bricks, and adobe units.

Type of unit	Specimen	Dimensions (mm^3)	Compressive strength (MPa)
Old bricks	1	102 × 102 × 54	5.64
	2	102 × 101 × 52	6.85
	3	100 × 102 × 50	13.46
	4	102 × 101 × 54	8.08
	5	103 × 102 × 52	7.81
	6	103 × 100 × 54	9.33
		Mean = 8.53 CV = 31.80 %	
Contemporary bricks	1	210 × 117 × 86	6.20
	2	212 × 117 × 85	3.61
	3	216 × 116 × 81	7.57
	4	212 × 114 × 83	7.31
	5	215 × 117 × 84	4.25
		Mean = 5.79 CV = 30.96 %	
Adobe units	1	207 × 105 × 110	0.63
	2	108 × 105 × 107	0.50
	3	109 × 109 × 108	0.61
	4	118 × 109 × 107	0.54
	5	103 × 106 × 105	0.57
	6	105 × 108 × 112	0.53
		Mean = 0.56 CV = 8.82 %	

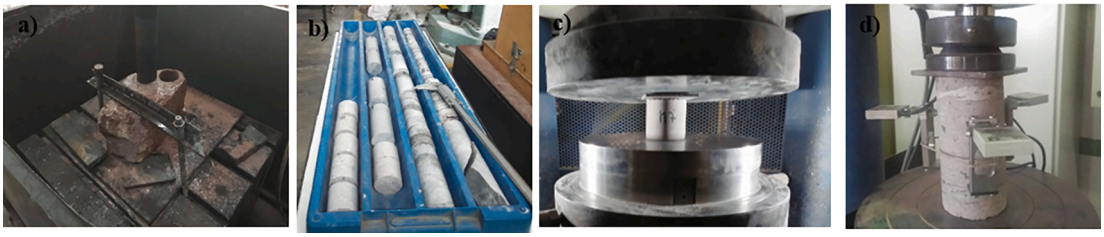

Fig. 14. a) Core drilling of cylindrical specimens from remains of Inca stone blocks, b) core samples obtained, c) compression test, and d) evaluation of Young's modulus at UPC laboratory.

were obtained from remains of original Inca stone blocks collected inside the historical site. The measured density of the stone was 2,290 kg/m^3. The average compressive strength was 96.9 MPa (CV = 15.8 %) for specimens tested at PUCP, and 118.4 MPa (CV = 20.2 %) for samples tested at UPC. One of the specimens tested at the UPC was used to evaluate Young's modulus, yielding a value of 26,653 MPa. Table 2 presents a summary of the results for all the specimens tested.

5.5. *Mortar*

Small lime and cement mortar samples were extracted on site from old and contemporary masonry respectively, and were tested according to the double punch test setup [85] by applying a loading rate of 1 kN/min, see Fig. 15. Lime mortar joint specimens provided a mean compression strength of 5.31 MPa (CV = 55.40 %). In contrast, cement mortar joint specimens provided a mean compression strength of 8.27 MPa (CV = 13.33 %). Table 3 presents a summary of the results for all the samples tested.

6. Structural analysis

6.1. *Description of the numerical model and materials properties*

The investigation of the seismic performance of the Huaytará-Huancavelica church was performed through a non-linear finite element analysis using the software DIANA-FEA [86]. The structural model was prepared using the 3D geometry obtained through photogrammetry, as described in Section 4. As in-situ inspection revealed that the flexible timber roof of the main nave and the sacristy is connected with the surrounding walls only through friction connections, the roofs were not included in the model. Still, their weight was considered as a distributed load of 7.2 kN/m^2 at the top of the surrounding walls of the main nave. Separate analyses were carried out for the nave and the towers for two reasons. First, as the towers were a posterior addition, there is a visible physical separation between them and the nave and, therefore, no proper connection, as confirmed by the in-situ inspection. Second, the separate analysis of each element permitted us to obtain the full force vs. displacement response under the local failure mechanism. For all cases, the

Table 2
Summary of compression tests results from stone specimens.

Laboratory	Specimen	Diameter(mm)	Height(mm)	Compressive strength(MPa)
PUCP – Peru	A	55.4	116.8	94.42
	B	55.3	115.7	88.23
	C	55.3	116.5	92.31
	1A	55.5	116.4	82.72
	1B	55.3	117.3	108.24
	1C	55.5	118.0	126.52
	2A	55.5	116.2	77.05
	2B	55.5	116.2	93.27
	2C	55.3	115.4	109.47
		Mean = 96.91 CV = 15.80 %		
UPC – Barcelona	P_01	55	55	130.11
	INCA_01	55	55	166.35
	INCA_02	55	55	139.17
	INCA_03	55	55	102.73
	INCA_04	55	55	153.25
	INCA_05	55	55	104.39
	INCA_06	55	55	104.75
	INCA_07	55	55	108.84
	INCA_08	55	55	79.43
	INCA_09	55	55	106.28
	INCA_10	55	55	107.44
	INCA_11	55	55	129.72
	INCA_12	55	55	106.40
		Mean = 118.37 CV = 20.20 %		

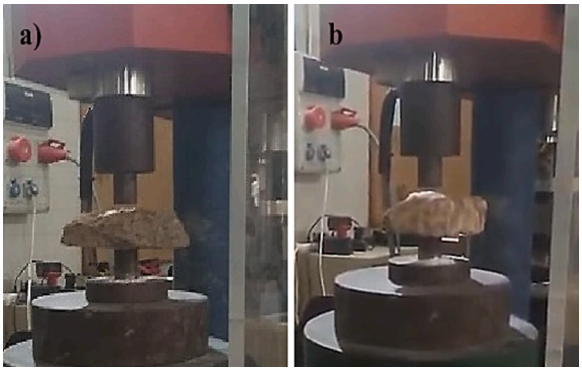

Fig. 15. Double punch test on mortars according to DIN 18555-9 [85] on a 10 kN capacity loading machine (Ibertest). a) Old lime mortar test, and b) contemporary cement mortar.

only boundary conditions are the constraints of all movements at the base of the walls and not considered the interaction among them.

Fig. 16 presents the finite element mesh of the 3D model, which is composed of 38 solids according to the material Fig. 6, that contains 746,472 isoparametric 4-node tetrahedral elements (TE12L). The side-length of the finite elements is between 0.1 m and 0.6 m, Furthermore, a higher concentration of elements is observed at the top of the tower to accurately represent its irregular geometry and ensure the convergence of the numerical model.

All the analyses considered geometrical and material nonlinearity. The numerical solution of the discrete problem was solved at each step of the analysis through a Quasi-Newton method, and the convergence was checked based on an energy norm using a threshold of 10^{-3} [86]. The non-linear behaviour of masonry was represented using the smeared crack Total Strain Rotating Crack Model (TSRCM) implemented in DIANA FEA [86].

Table 4 presents the properties of the materials in the temple and the towers. While the location of cracks has been identified with the use of photogrammetry, these are not included in the numerical model due to the lack of in-situ experimental testing that would allow the estimation of local changes in the material properties. This can be achieved in future investigations through the use of dynamic identification techniques and a manual mapping of cracks, as shown in [87,88], while an automatic mapping of damage on the geometrical model based on photogrammetry has been recently presented in [89].

The compressive and tensile fracture energies for all the materials were computed using the following two expressions [90], which enable a direct correlation between strength and fracture energies:

Table 3
Summary of double punch tests results from mortar joint specimen.

Type of mortar	Specimen	Thickness(mm)	Height(mm)	Compressive strength (MPa)
Cement	DPT_CEMT_01	20.0	314.0	9.35
	DPT_CEMT_02	17.0	314.0	7.79
	DPT_CEMT_03	16.0	314.0	8.98
	DPT_CEMT_04	15.0	314.0	6.95
	Mean = 8.27 CV = 13.33 %			
Lime	DPT_CAL_01	29.0	314.0	9.84
	DPT_CAL_02	28.5	314.0	3.16
	DPT_CAL_02_TRO_02	30.0	314.0	6.87
	DPT_CAL_02_TRO	27.0	314.0	7.42
	DPT_CAL_05	14.0	314.0	4.42
	DPT_CAL_06	17.0	314.0	8.39
	DPT_CAL_07	17.0	314.0	3.76
	DPT_CAL_08	11.0	314.0	0.97
	DPT_CAL_09	10.0	314.0	2.94
	Mean = 5.31 CV = 55.40 %			

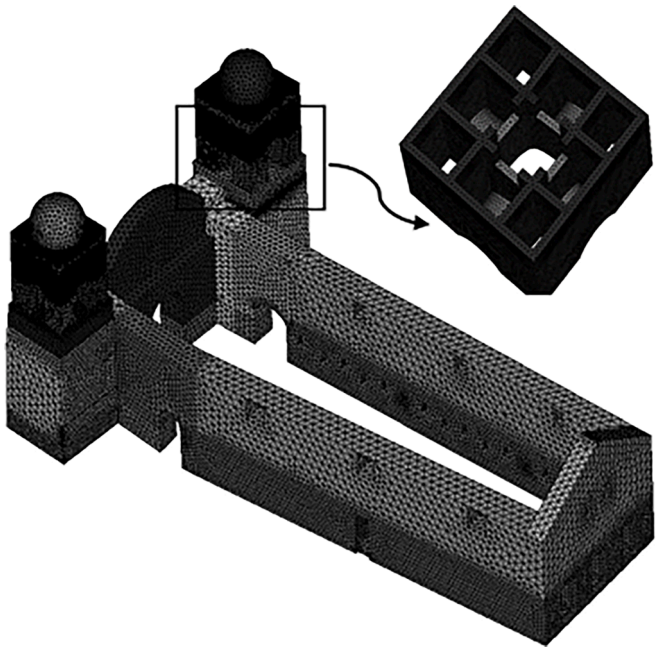

Fig. 16. Finite element model and mesh used in the numerical analysis. The top right figure shows a detail of the mesh of the interior of the towers supporting the domes.

Table 4
Material properties used in the numerical analyses.

Material	Density [kg/m^3]	Young's modulus, E [MPa]	Poisson's ratio[-]	f_c[MPa]	f_t[MPa]	G_{fc}[N/m]	G_{ft}[N/m]
Ancient brick masonry	1,800	935	0.25	1.7	0.085	2,720	7.12
Contemporary brick masonry	1,800	1,780	0.25	3.24	0.16	5,186	11.19
Adobe masonry	2,000	200	0.2	0.45	0.04	155	10
Inca Stone masonry	2,290	26,653	0.25	11.48	0.57	18,368	16
Colonial Stone masonry	2,140	2,340	0.25	3	0.15	4,800	4.35
Rubble stone masonry	1,900	330	0.25	0.6	0.03	1,500	10
Concrete C12	2,350	27,088	0.2	20	1.57	32,000	125.7

$$G_{ft} = 0.04 f_t^{0.7} \tag{1}$$

$$G_{fc} = df_c \tag{2}$$

With a ductility index d = 1.6 mm in Eq. (2) following [91]. Unless differently stated, for materials that had not been referenced in the literature, Young's modulus E was computed as a function of the compressive strength f_c by using the relationship $E = 550\, f_c$ [90]. The same stands for the tensile strength, defined as 5 % of the compressive one.

The selection of the rest of the mechanical properties for each material is described in the following subsections.

In the case of adobe, the average compressive strength obtained from tests on adobe cubes (see Section 5) was 0.56 MPa. This value is close to the results reported in the literature for adobe walls in Peru, which range between 0.45 and 1.64 MPa [92–94]. However, laboratory tests on cubic specimens neglect the presence of joints in adobe walls, which are expected to reduce further their actual compressive strength. For this reason, a compressive strength of 0.45 MPa was selected in agreement with Tarque et al. [95,96]. The tensile strength was defined as 10 % of the compressive one [95] , while Young's modulus was considered equal to 200 MPa ([95], Norma Peruana E.80 [80]).

In both contemporary and ancient brick masonry, a unified approach has been adopted, treating them as a composite and homogeneous material. The determination of the properties of this material is derived from the mechanical characteristics of both mortar and brick, following the guidelines of Eurocode 6 and according to Eq. (3).

In the case of the contemporary brick masonry, the compressive strength was computed equal to 3.24 MPa according to the expression of Eurocode 6 [97],

$$f_c = K f_{bc}^{0.7} f_{mc}^{0.3} \tag{3}$$

where f_{bc} and f_{mc} are the brick and the mortar compressive strengths, respectively, as obtained by the experimental tests presented in Section 5, K is a constant equal to 0.55 for clay bricks [97]. This value of 3.24 MPa (f_{bc}) and 0.16 MPa (f_{mc}) were within the limits given by the Peruvian standard [79] and other national standards [98,99]. Finally, a density of 1,800 kg/m^3 was defined according to [100].

In the case of ancient brick masonry, the compressive strength given by Eq. (3) is equal to 3.39 MPa, considering the experimentally obtained compressive strengths of the brick and mortar, as derived in Section 5. The density was 1,800 kg/m^3, equal to the value used for a similar masonry typology in [25].

In the case of Inca stone masonry, made of large subvolcanic, intrusive igneous rock (Microdiote) carved into polyhedral shapes that fit perfectly and exquisitely with the neighbouring ones, the compressive strength is 95.52 MPa (see Section 5). The result of this construction practice is solid walls without any mortar. This ingenious construction typology based on the complex interlocking between blocks enhances the resistance of the walls. Experimental tests of this masonry typology are scarce in the literature [101,102], while research shows that dry stack masonry with smooth surfaces, such as the Inca one, has superior compressive strength compared to masonry with the same stone and mortar joints [103]. Considering the superior compressive strength of dry stack masonry, the compressive strength of the Inca masonry in this work was defined as equal to 11.48 MPa, corresponding to the highest value proposed by the Italian standards for squared stone masonry considering the coefficients of 1.4 [99]. The Young's modulus corresponding to this masonry typology equals 26,653 MPa, as obtained experimentally. The chosen value of the density is equal to the stone one measured in laboratory (Section 5).

In the case of Colonial stone masonry, the compressive strength and Young's modulus of the colonial ashlar stone masonry were defined following the same procedure as Lourenco et al. [49] for the analysis of *Casa Arones* building at Cusco, which features the same masonry typology. Both values fall within the range proposed by OPCM 3431 [104] and NTC [100] standards. The density value is also the same as that used for the analysis of the *Casa Arones* [49].

In the case of rubble stone masonry, used in the colonial time in the church's sacristy, the compressive strength and Young's

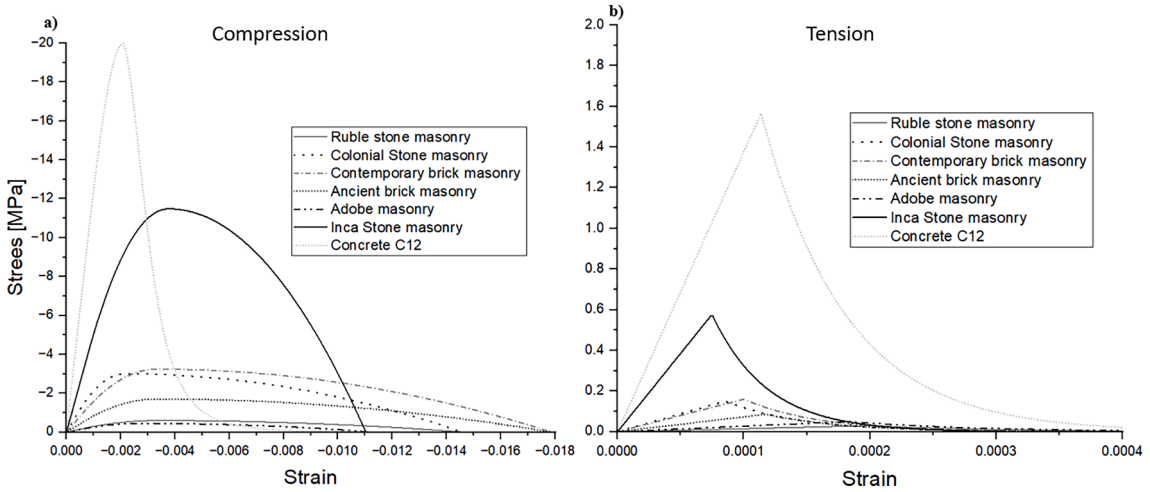

Fig. 17. Stress–strain relationships depicting constitutive law curves for (a) compression and (b) tension across all materials used in the study.

modulus were defined following the suggestions of existing codes and considering the relevant literature on similar structures. In particular, a value of $f_c = 0.6$ MPa and $E = 330$ MPa (i.e. $E = 550\ f_c$ [90]) were considered, similarly as the values of [49]. The compressive strength value corresponds to the minimum reference value of OPCM 3431 [104].

In the case of concrete, owing to the lack of experimental evidence on the mechanical properties of the elements at the two towers (slabs and rings), their mechanical properties were selected conservatively equal to a C12 typology of Eurocode 2 [105]. The curves of the constitutive laws for all church materials are shown in Fig. 17a for compression and Fig. 17b for tension.

6.2. Numerical analysis and seismic vulnerability

The seismic behaviour was analysed using a non-linear pushover analysis, and the seismic performance was evaluated using a displacement-based approach (N2 method). The analysis was conducted using DIANA FEA®, a finite element-based software, with incremental lateral load analysis. For the nave, four analyses were performed by considering loading in all directions perpendicular to the perimeter walls, see Fig. 18. For the towers, we performed two analyses corresponding to the directions pushing towards the free sides, i.e. North and East for the North tower and South and East for the South tower. All the analyses were performed in two steps, including applying the self-weight at the first step and the incremental application of the horizontal forces proportional to the mass distribution in the second one.

In addition, a modal analysis has been performed and is visualised in Fig. 19. Fig. 19a presents the four initial nodes of the church ranging from 2.69 Hz to 3.10 Hz. Furthermore, Fig. 19b and Fig. 19c shows the first five modes of vibration of the north and south tower respectively, where the period ranges between 1.87 and 8.32 Hz and between 1.98 and 6.67 Hz for the south tower.

Among the four considered loading cases for the analyses of main nave, the lowest base shear corresponds to loading towards the South direction, with damage affecting mainly the western façade, see Fig. 20c. For loading towards the west (Fig. 20a), vertical cracks appear at the adobe walls along the connections of the façade with the transversal walls at the same location where cracks appear today in the structure (see Section 3.3), and horizontal cracks at the interface with the Inca stone masonry. Cracking also occurs at the base of the gable in the eastern façade, but to a lesser extent than the western one. Damage at the eastern façade is more prominent for loading towards the East (Fig. 20b). The adobe walls present substantial vertical cracking at the connections with the transverse walls and above the door and window openings. Horizontal cracks appear at two locations, i.e. at the interface with the stone masonry at the base and at the height where the width of the façade decreases.

The damage in the structure for loading towards the South-North direction are similar to each other (Fig. 20c-d), affecting mainly the southern and eastern walls. In these cases, horizontal cracking occurs at the interface between the adobe walls and the Inca stone masonry, overturning the former. For loading towards the south, cracks appear at the intersection between orthogonal walls, which are visible today. Some cracking is also present at the eastern façade above the openings. The smaller thickness of the southern wall results in the earliest initiation of its out-of-plane failure when loading towards the south. This justifies the lowest acceleration capacity among the four studied cases.

Fig. 21 presents the results of the pushover analyses of the main nave in terms of base shear vs. displacement capacity curve. The maximum base shear was very similar for all four loading directions, with values ranging between 220 and 240 kN. For all the cases, the structure's response is characterised by an approximately linear branch, followed by a parabolic branch up to the maximum capacity. The post-peak response is characterised by a sudden drop for the east, south and north loading directions occurring in a single analysis step. For the west loading direction, the post-peak response is characterised by a more gradual loss of capacity.

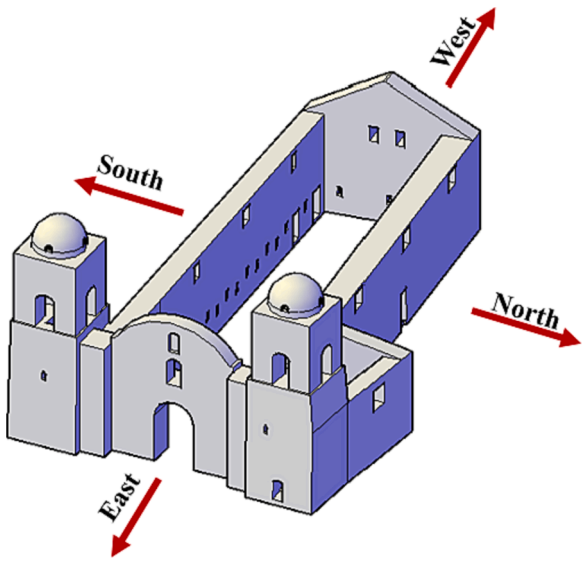

Fig. 18. The four loading directions of the pushover analyses.

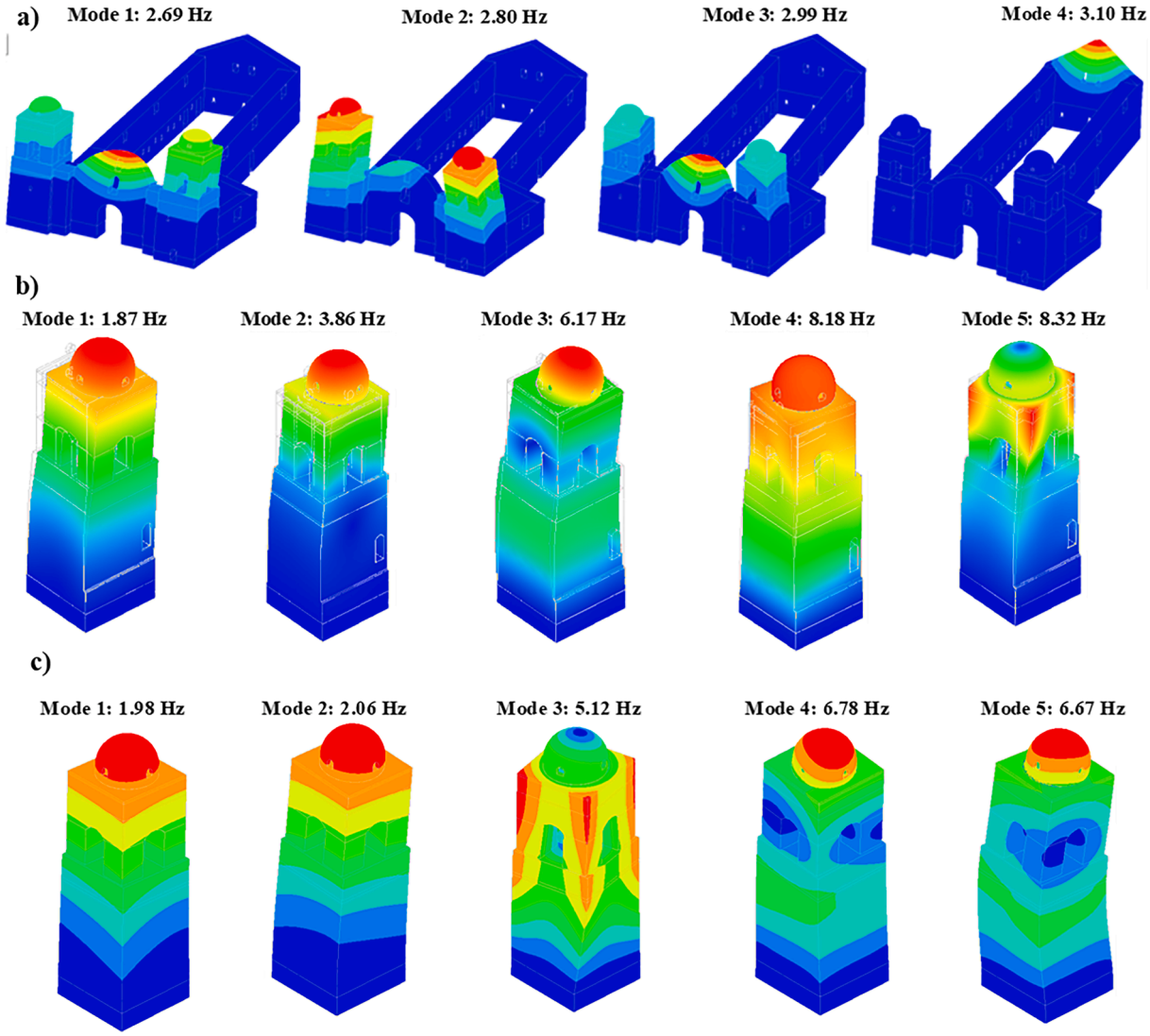

Fig. 19. Modal shapes obtained from numerical models representing (a) the first four modes of the nave of the church, (b) the first five modes of the north tower, and (c) the first five modes of the south tower.

Fig. 22a and b present the capacity curves and the cracking distribution for the South and North tower pushover analyses, respectively. The seismic response of the two towers is very similar in strength capacity and damage distribution. The capacity of the northern tower is slightly lower than that of the southern one, which could be related to the smaller effective section on the north tower due to the larger internal open volume for the staircase. The base shear capacity of the two towers is much lower than that of the temple's nave, as presented previously. The capacity curves of the towers present a linear branch up to approximately 80 % of the maximum strength. This is followed by a short parabolic hardening part up to the maximum strength. The post-peak part presents a softening behaviour, with a critical strength decrease for increasing displacement. For all the cases, the numerical analyses could continue up to a 20 % drop in the strength.

The towers behaved as a cantilever and developed a flexural overturning mechanism characterised by important cracking at the interface between stone and adobe masonry (see Figures Fig. 23 and Fig. 24) for all analysed cases. The northern tower's northern wall also presents important vertical cracking in the interior at the location of the internal staircase, which was also observed during the in-situ inspection (see Section 3.3). Similar damage does not appear in the southern tower due to the limited width of the staircase compared to that of the northern tower. Compressive damage was also observed at the base of the adobe walls, which started appearing close to the peak base shear and interior corridor of the north tower, see Figures Fig. 23c and Fig. 24c.

6.3. Displacement-based assessment – N2 method

The most vulnerable parts of the structure were identified using the N2 method developed by Fafjar and Fischinger in 1988 [106]

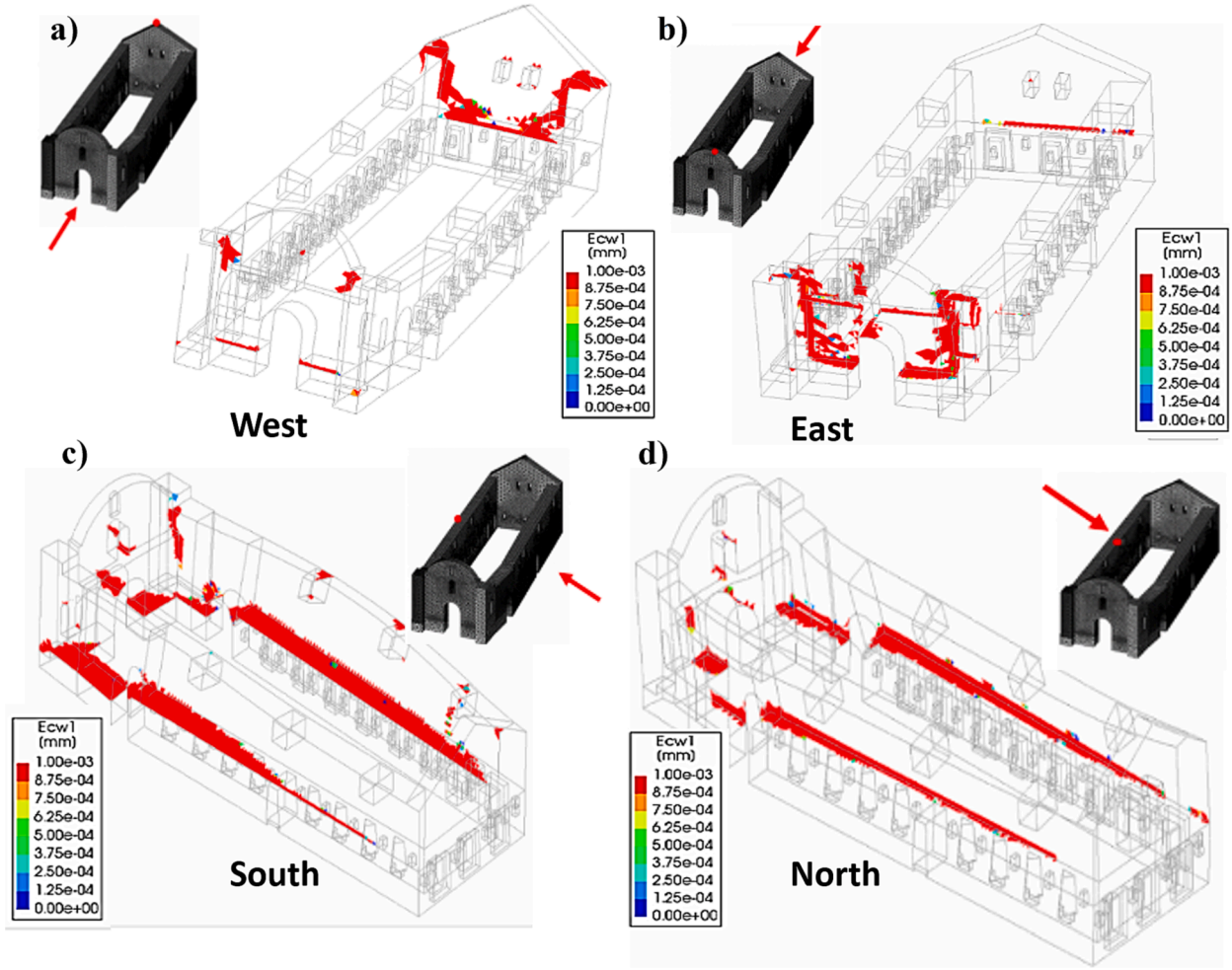

Fig. 20. Distribution of the crack width for the four pushover analyses of the main nave: (a) West direction, (b) East direction, (c) South direction, and (d) North direction.

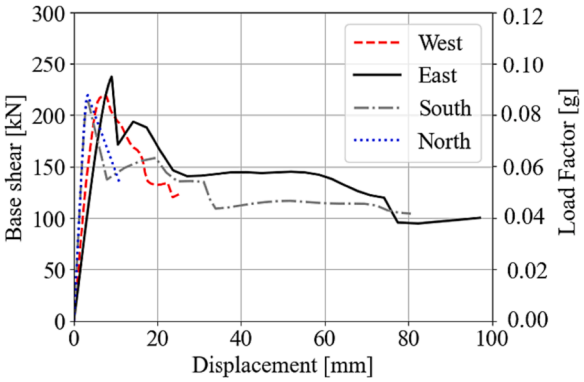

Fig. 21. Pushover curves base shear – horizontal displacement for the main nave.

and later implemented in Eurocode 8 [107], among other standards. The N2 method has been applied in the numerical analysis of some complex structures obtaining adequate responses in terms of collapse mechanisms, verification of seismic performance through the evaluation of the displacement demand on the capacity curve [37,108–113]. However, it is acknowledged that pushover analysis based on a single loading pattern ignores the effect of higher modes, which could be play an important role in slender structures such as

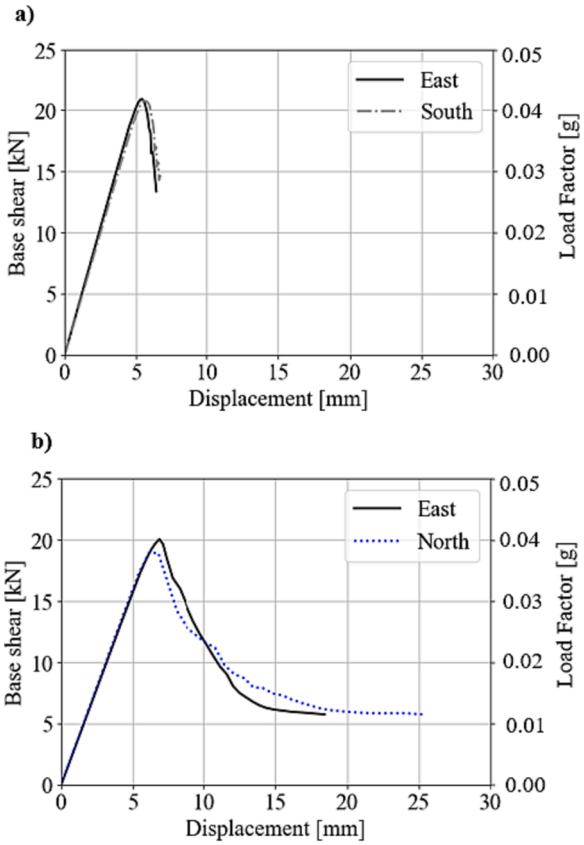

Fig. 22. Pushover curves of base shear – horizontal displacement: a) East and South direction on South tower, and b) East and North direction on North tower.

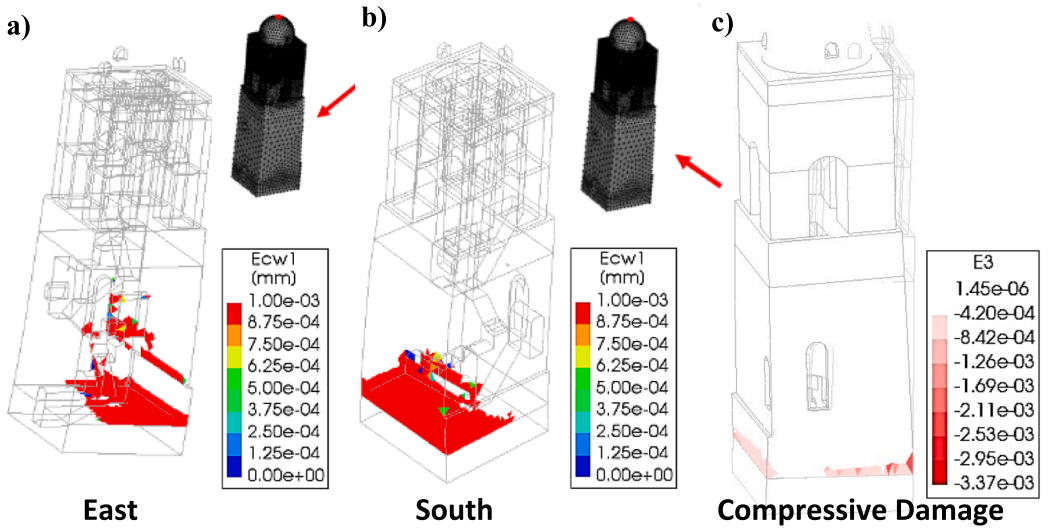

Fig. 23. Failure mechanism for the north tower: a) Crack width for the east direction, b) crack width for the east direction, and c) compression damage in the interior corridor of the north tower, showing considerable deformation at the base of the adobe structure.

towers [114].

For each analysis direction, we obtained the PGA, which leads to the maximum displacement capacity, conventionally defined as the displacement corresponding to a 20 % drop in the horizontal strength. In this way, a quantitative comparison between the seismic

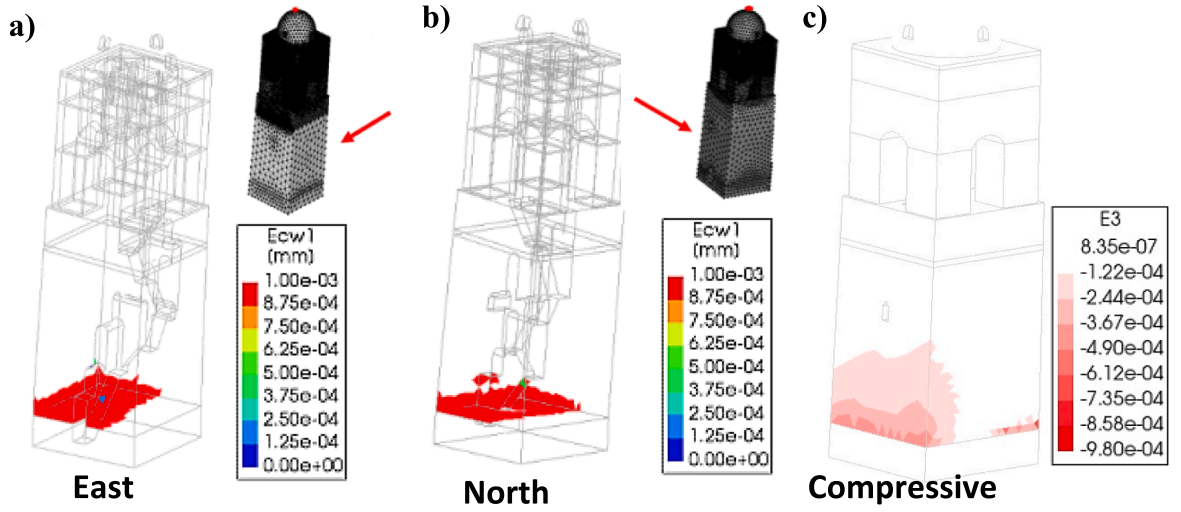

Fig. 24. Failure mechanism for the Southern tower: a) crack width for the east direction, b) crack width for the north direction, and c) compression damage in the interior corridor of the south tower, showing deformation at the base of the adobe structure.

demand necessary to result in a collapse for different loading directions can be identified.

The reference elastic spectra are one of the Peruvian seismic standards E.030 for a return period of 475 years [115]. This was defined by assuming a 5 % damping factor corresponding to the geographical position of the site (Zone 4, Z = 0.45 g), soil type S3 Soft Soils (S = 1.10, T_p = 1.00 and T_L = 1.60), Seismic Amplification Factor C = 2.5, category of use C (U = 1.00), and seismic reduction coefficient R = 1. This spectrum corresponds to the PGA acceleration of the reference site, see Fig. 23. When implementing the N2 method, we down-scaled the spectrum by changing the PGA to find the one that results in the conventional collapse of the structure. Fig. 25 shows an example of the computation of the PGA corresponding to the collapse of the nave when loaded towards the south.

The bilinear curve for each analysis was computed considering as stiffness the secant stiffness corresponding to 70 % of the maximum strength given by the pushover analysis and as ultimate displacement the one corresponding to a 20 % drop in the strength. The maximum force is then defined to ensure that the area below the bilinear and pushover curve is the same.

Table 5 presents the PGA values resulting in target displacement equal to the yield displacement and the ultimate displacement (collapse) for different loading directions of the main nave, south tower and north tower, respectively. The results show that the most vulnerable parts of the nave are the south and north facades for a loading direction South-North, with a PGA leading to collapse equal to approximately 0.21 g. The PGA leading to a target displacement equal to the yield displacement of the bilinear curves is also the lowest for these two facades for loading towards South-North, equivalent to 0.17 g. The towers show a much lower capacity, with PGA leading to the collapse of 0.09 g and PGA corresponding to a yield of 0.08 g.

During the 2007 Pisco earthquake, which occurred 150 km away from Huaytara the San Juan Bautista church experienced localised damage in the North tower, resulting in the collapse of the dome, as depicted in Fig. 5e. Specifically, the top part of the north tower collapsed, and cracks appeared at the connection with the neighbouring walls of the nave. Additionally, there is no record of PGA in the area. The pushover analysis with a loading pattern proportional to the mass distribution could not represent this type of failure. There are two potential reasons for this. First, the interaction of the towers with the adjacent nave influences their dynamic response, which

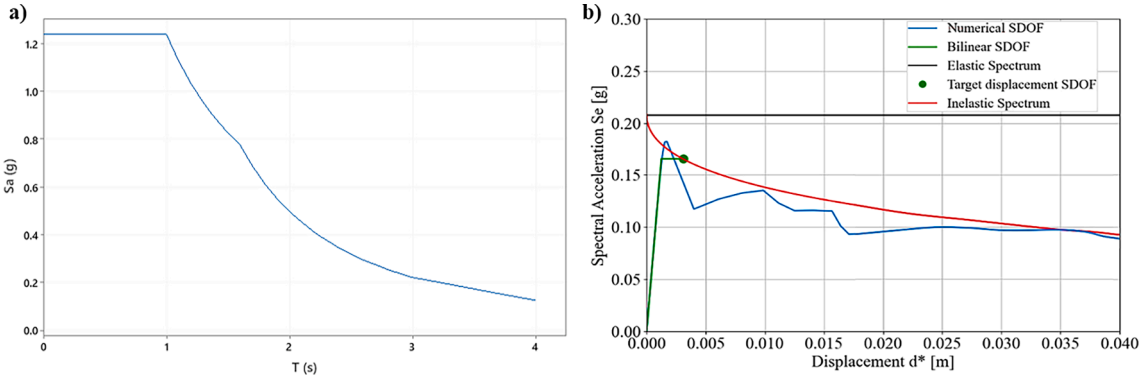

Fig. 25. a) Peruvian seismic standards E.030 to Huaytara in Acceleration – Period, and b) Application of the N2 method for estimating the PGA leading to the collapse of the nave when loaded towards south. Curves correspond to the equivalent Single Degree of Freedom (SDOF) system.

Table 5
Summary of the PGA values resulting in target displacement equal to the yield displacement and the ultimate displacement (collapse) for different loading directions of the main Nave, South tower and North tower .

Main nave			South tower			North tower		
Loading direction	PGA corresponding to yield [g]	PGA for collapse [g]	Loading direction	PGA corresponding to yield [g]	PGA for collapse [g]	Loading direction	PGA corresponding to yield [g]	PGA for collapse [g]
West + X	0.40	0.50	East -X	0.08	0.09	East -X	0.09	0.10
East -X	0.38	0.47	South + Y	0.08	0.09	North -Y	0.08	0.09
South + Y	0.17	0.21						
North -Y	0.17	0.22						

could be better represented with a dynamic time history analysis of the whole structure (nave with towers). Secondly, during the in-situ inspection, it became evident that a weak interface existed between the dome and the south tower. This issue arose due to the absence of anchorage while constructing the dome's base with the tower. Given the structural similarities between the two towers, it was inferred that the north tower also had a similar interface (see Fig. 26 and Fig. 5d). Simulating this structural interface necessitates information about the properties of the interface between the dome and the underlying material. Unfortunately, such information was unavailable because the section of the north tower in question had been reconstructed after the 2007 earthquake.

7. Conclusions

The paper has presented a cost-effective methodology for the digital survey and numerical assessment of historical structures based on photogrammetry. The method is demonstrated through its application to the seismic assessment of a symbolic case study; the San Juan Bautista church – Inca Temple of Huaytará, Peru. To the knowledge of the authors, this is the first numerical assessment of a complex structure featuring adobe-brick-stone masonry.

The methodology begins with a comprehensive historical survey of the construction phases of the heritage complex. Subsequently, the 3D geometrical model is derived and the current pathology is identified based on structure-from-motion photogrammetry. This is followed by the characterisation of the construction materials through in-situ field work and laboratory experimental tests in PUCP (Lima, Peru) and UPC (Barcelona, Spain). In the final step, this information is used to prepare the numerical model and run a displacement-based assessment under seismic loading.

The model is composed by various masonry types including adobe masonry, contemporary brick masonry, ancient brick masonry, Inca stone masonry, colonial stone masonry, and rubble stone masonry, as well as concrete elements, each assigned with different material properties. The mechanical properties were determined based on laboratory tests and using relationships in codes and relative literature.

Non-linear analyses were executed considering gravitational actions and earthquake-equivalent static loading. For the main nave, four pushover analyses were conducted corresponding to four directions perpendicular to the perimeter walls. The analyses confirmed that damage-prone areas are the connections between different masonry types and the interface of adobe with the Inca stone masonry.

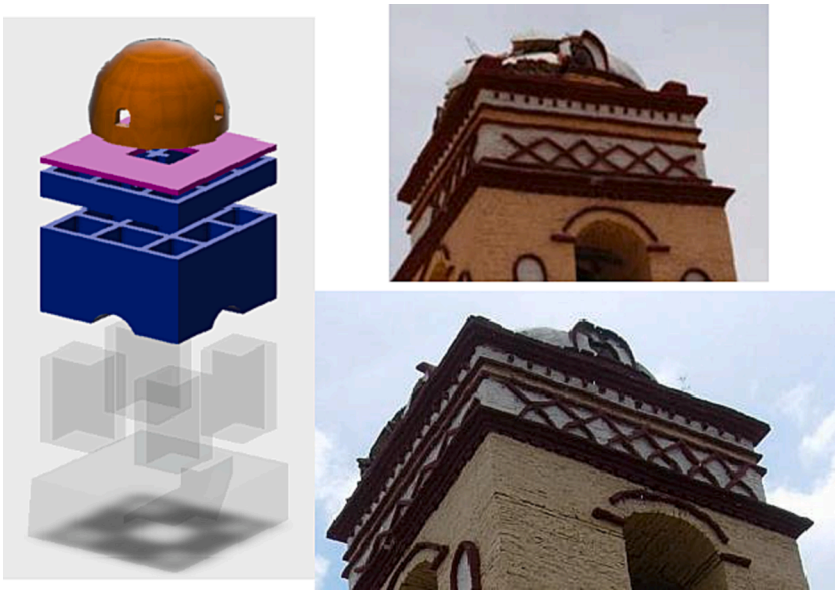

Fig. 26. Platform constructed as basement of the dome and collapsed dome of the North tower.

For the towers, analyses were carried out in two directions, i.e. East and South for the South tower, and East and North for the North tower, respectively. In this case, the analyses resulted in flexural overturning mechanisms and cracking at the interface between stone and adobe masonry.

The seismic performance of the main nave and the towers was analysed by using the N2 method. The results show that the most vulnerable parts of the nave are the south and north facades with a PGA leading to collapse equal to 0.21 g. The towers show a much lower capacity, with PGA leading to the collapse of 0.09 g.

This work shows how photogrammetry can aid the generation of geometrical models of existing structures, as well as the documentation and visualisation of the existing condition and pathology. Overall, the numerical analysis provided insights into the seismic performance of the Huaytará-Huancavelica church and the vulnerability of its different structural elements. The results can be used to assess the church's structural integrity and inform potential retrofitting or preservation measures. Along this line, in-situ testing such as dynamic identification would allow the calibration of the developed model and the incorporation of existing damage through a modal updating approach. Moreover, a more thorough investigation of the seismic behaviour of the church with time-history analysis would help to identify any effect of higher modes that could lead to the local collapse of one of the two towers. This information is necessary in order to assess possible retrofit strategies that will improve the seismic resistance of this valuable monument.

CRediT authorship contribution statement

Emerson Cuadros-Rojas: Data curation, Formal analysis, Funding acquisition, Investigation, Software, Validation, Visualization, Writing – original draft. **Savvas Saloustros:** Conceptualization, Methodology, Data curation, Formal analysis, Investigation. **Nicola Tarque:** Conceptualization, Investigation, Methodology, Resources, Software, Supervision, Validation, Writing – review & editing. **Luca Pelà:** Conceptualization, Methodology, Funding acquisition, Investigation, Project administration, Resources, Supervision, Writing – original draft, Writing – review & editing.

Declaration of competing interest

The authors declare that they have no known competing financial interests or personal relationships that could have appeared to influence the work reported in this paper.

Data availability

Data will be made available on request.

Acknowledgments

The authors gratefully acknowledge the financial support from the Ministry of Science, Innovation and Universities of the Spanish Government (MCIU), the State Agency of Research (AEI), as well as that of the ERDF (European Regional Development Fund) through the project SEVERUS (Multilevel evaluation of seismic vulnerability and risk mitigation of masonry buildings in resilient historical urban centres, ref. num. RTI2018-099589-B-I00). The first author gratefully acknowledges the AGAUR agency of the Generalitat de Catalunya for the financial support of his predoctoral grant, the PRONABEC program by the Peruvian Government for the financial support of his master studies and the in-situ activities of the research, and Oliver Cuadros for his support in the photogrammetric modelling.

The authors also thank Prof. Daniel Torrealva from the laboratory of antiseismic structure of PUCP, Farley Munares from the laboratory of mines of PUCP, Florencio Torres head of the archaeological site of Huaytará, Julio Cuadros and Oliver Cuadros for his great help in the development of the architectural perspectives, and Alejandro Saldaña the parish priest of the church of San Juan Bautista in Huaytará.

References

[1] F. Parisi, N. Tarque, H. Varum, J. Vargas-Neumann, Adobe constructions in the world: a first overview, in: H. Varum, F. Parisi, N. Tarque, D. Silveira (Eds.), Structural Characterization and Seismic Retrofitting of Adobe Constructions. Building Pathology and Rehabilitation, Springer, Cham, 2021, pp. 1–14, https://doi.org/10.1007/978-3-030-74737-4_1.

[2] A. Sánchez, H. Varum, T. Martins, J. Fernández, Mechanical properties of adobe masonry for the rehabilitation of buildings, Constr. Build. Mater. 333 (2022), https://doi.org/10.1016/j.conbuildmat.2022.127330.

[3] W.S. Ginell, E.L. Tolles, Seismic stabilization of historic adobe structures, J. Am. Inst. Conserv. 39 (2000) 147–163, https://doi.org/10.1179/019713600806113257.

[4] A. Preciado, A. Ramirez-Gaytan, J.C. Santos, O. Rodriguez, Seismic vulnerability assessment and reduction at a territorial scale on masonry and adobe housing by rapid vulnerability indicators: The case of Tlajomulco, Mexico, Int. J. Disaster Risk Reduct. 44 (2020) 101425, https://doi.org/10.1016/J.IJDRR.2019.101425.

[5] A. Preciado, J.C. Santos, A. Ramirez-Gaytan, K. Ayala, J.de.J. Garcia, A correlation between moisture and compressive strength of a damaged 15-year-old rammed soil house, Geomech. Eng. 23 (2020) 227–244.

[6] A. Preciado, J.C. Santos, C. Silva, A. Ramírez-Gaytán, J.M. Falcon. Seismic damage and retrofitting identification in unreinforced masonry Churches and bell towers by the september 19, 2017 (Mw = 7.1) Puebla-Morelos earthquake. Eng. Fail. Anal. 118;2020:104924, doi:10.1016/j.engfailanal.2020.104924.

[7] X. Cárdenas-Haro, L. Todisco, J. León, C. Jurado, E. Vergara, Geometry and Proportions of Adobe Vernacular Buildings in Cuenca, Ecuador, Int. J. Archit. Heritage 16 (2022) 1270–1288, https://doi.org/10.1080/15583058.2021.1879312.

[8] P. Baquedano-Juliá, T.M. Ferreira, C. Arriagada-Luco, C. Sandoval, N.C. Palazzi, D.V. Oliveira, Multi-vulnerability analysis for seismic risk management in historic city centres: an application to the historic city centre of La Serena, Chile, Nat. Hazards (2023) 1–44, https://doi.org/10.1007/S11069-023-06008-8.

[9] H. Varum, N. Tarque, D. Silveira, G. Camata, B. Lobo, M. Blondet, et al.. Structural Behaviour and Retrofitting of Adobe Masonry Buildings BT – Structural Rehabilitation of Old Buildings, Springer Berlin Heidelberg, Berlin, Heidelberg, 2014, pp. 37–75, https://doi.org/10.1007/978-3-642-39686-1_2.

[10] G. Sumerente, H. Lovon, N. Tarque, C. Chácara, Assessment of combined in-plane and out-of-plane fragility functions for adobe masonry buildings in the peruvian andes, Front. Built. Environ. 6 (2020) 1–10, https://doi.org/10.3389/fbuil.2020.00052.

[11] R. Illampas, I. Ioannou, D.C. Charmpis, A study of the mechanical behaviour of adobe masonry, WIT Trans. Built Environ. 118 (2011) 485–496, https://doi.org/10.2495/STR110401.

[12] M. Dormohamadi, R. Rahimnia, Combined effect of compaction and clay content on the mechanical properties of adobe brick, Case Stud. Constr. Mater. 13 (2020) e00402.

[13] C.H. Kouakou, J.C. Morel, Strength and elasto-plastic properties of non-industrial building materials manufactured with clay as a natural binder, Appl. Clay Sci. 44 (2009) 27–34, https://doi.org/10.1016/j.clay.2008.12.019.

[14] D. Silveira, H. Varum, A. Costa, T. Martins, H. Pereira, J. Almeida, Mechanical properties of adobe bricks in ancient constructions, Constr. Build. Mater. 28 (2012) 36–44, https://doi.org/10.1016/j.conbuildmat.2011.08.046.

[15] S. Lenci, E. Quagliarini. Mechanichal Haracterization of Some Roman Adobe Masonries At the Archaeological Site of Suasa (an). SMC Magazine n.d.:12–7.

[16] D. Liberatore, G. Spera, M. Mucciarelli, M.R. Gallipoli, D. Santarsiero, C. Tancredi, Typological and experimental investigation on the adobe buildings of Aliano (Basilicata, Italy), Structural Analysis of Historical Constructions Constructions (2006) 851–858.

[17] E. Baglioni, F. Fratini, L. Rovero, the Materials Utilised in the Earthen Buildings Sited in the Dràa Valley (Morocco), Mineral. Charact. (2010) 1–10.

[18] Jin-sheng Huang, Tao Zhong, PW Lu Kun, Experiment on Mechanics Characteistics of Adobe Masonry of Rural Houses in Yunnan Province, Earthquake Resistant Engineering and Retrofitting 30 (1) (2008).

[19] Z. Li, M. Noori, A.W. Altabey, Experimental and numerical assessment on seismic performance of earth adobe walls, Struct. Durab. Health Monit. 15 (103–23) (2021), https://doi.org/10.32604/sdhm.2021.011193.

[20] R. Arroyo Matus, S. Sánchez Tizapa, Q.P. Catalán, Caracterización experimental de las propiedades mecánicas de la mampostería de adobe del sur de México Characterization of the mechanical properties of southern Mexico's adobe masonry, Ingeniería 17 (2013) 167–177.

[21] D.M. Ruiz, N. Barrera, J.C. Reyes, M. Restrepo, Y.A. Alvarado, M. Lozada, et al., Strengthening of historical earthen constructions with steel plates: Full-scale test of a two-story wall subjected to in-plane lateral load, Constr. Build. Mater. 363 (2023) 129877, https://doi.org/10.1016/J.CONBUILDMAT.2022.129877.

[22] D.M. Ruiz, N. Barrera, J.C. Reyes, C. López, M. Restrepo, An approach to Colombian Andean earthen architecture in urban environments: a case study of Bogotá Historic Centre, J. Archit. Conserv. 29 (2023) 168–192, https://doi.org/10.1080/13556207.2022.2160556.

[23] J. Rivera, E. Muñoz. Caracterización Estructural de Materiales de Sistemas Constructivos en Tierra: El Adobe 2009:15.

[24] M. Blondet, J. Vargas, N. Tarque, C. Iwaki, Construcción Sismorresistente en tierra: la gran experiencia contemporánea de la Pontificia Universidad Católica del Perú (in Spanish), Informes De La Construccion 63 (2011) 41–50, https://doi.org/10.3989/ic.10.017.

[25] D. Torrealva, E. Vicente, T. Michiels, E. Colaboración, F. Greco, C. Cancino, et al.. Proyecto de Estabilización Sismorresistente Ensayo de materiales y componentes de la construcción de edifi cios históricos de adobe de Perú Informe de investigación, Getty Conservation Institute, 2019.

[26] B. Jiménez, L. Pelà, Numerical modelling of traditional buildings composed of timber frames and masonry walls under seismic loading, Int. J. Archit. Heritage (2022) 1–34, https://doi.org/10.1080/15583058.2022.2033885.

[27] B. Jiménez, S. Saloustros, L. Pelà, Seismic vulnerability index method for hybrid timber–masonry structures. Numerical calibration and application to the city of Valparaíso, Chile, J. Build. Eng. 44 (2021), https://doi.org/10.1016/j.jobe.2021.103185.

[28] M. Blondet, D. Torrealva, F. Ginocchio, J. Vargas, J. Velásquez. Seismic protection of earthen vernacular and historical constructions. Proceedings of the 10th International Conference on Structural Analysis of Historical Constructions. SAHC 2016 2016;7:3–14.

[29] ICOMOS, Recomendaciones para el análisis, conservación y restauración estructural del patrimonio arquitectónico. International Scientific Committee for Analysis and Restoration of Structures of Architectural Heritage, 2004.

[30] P. Roca, P.B. Lourenço, A. Gaetani. Historic construction and conservation: materials, systems and damage, Routledge (2019).

[31] G. Castellazzi, A.M. D'Altri, G. Bitelli, I. Selvaggi, A. Lambertini, From laser scanning to finite element analysis of complex buildings by using a semi-automatic procedure, Sensors (Switzerland) 15 (2015) 18360–18380, https://doi.org/10.3390/s150818360.

[32] A. Guarnieri, N. Milan, A. Vettore, Monitoring of complex structure for structural control using terrestrial laser scanning (Tls) and photogrammetry, Int. J. Archit. Heritage 7 (2013) 54–67, https://doi.org/10.1080/15583058.2011.606595.

[33] J. Martínez, A. Soria-Medina, P. Arias, A.F. Buffara-Antunes, Automatic processing of Terrestrial Laser Scanning data of building façades, Autom. Constr. 22 (2012) 298–305, https://doi.org/10.1016/j.autcon.2011.09.005.

[34] S. Saloustros, L. Pelà, P. Roca, J. Portal, Numerical analysis of structural damage in the church of the Poblet Monastery, Eng. Fail. Anal. 48 (2015) 41–61, https://doi.org/10.1016/j.engfailanal.2014.10.015.

[35] B. Conde, L.F. Ramos, D.V. Oliveira, B. Riveiro, M. Solla, Structural assessment of masonry arch bridges by combination of non-destructive testing techniques and three-dimensional numerical modelling: Application to Vilanova bridge, Eng. Struct. 148 (2017) 621–638, https://doi.org/10.1016/j.engstruct.2017.07.011.

[36] M.E. Stavroulaki, B. Riveiro, G.A. Drosopoulos, M. Solla, P. Koutsianitis, G.E. Stavroulakis, Modelling and strength evaluation of masonry bridges using terrestrial photogrammetry and finite elements, Adv. Eng. Softw. 101 (2016) 136–148, https://doi.org/10.1016/j.advengsoft.2015.12.007.

[37] C. Briceño, M.F. Noel, C. Chácara, R. Aguilar, Integration of non-destructive testing, numerical simulations, and simplified analytical tools for assessing the structural performance of historical adobe buildings, Constr. Build. Mater. 290 (2021), https://doi.org/10.1016/j.conbuildmat.2021.123224.

[38] M. Burgos, B. Castaneda, R. Aguilar, Virtual Reality for the Enhancement of Structural Health Monitoring Experiences in Historical Constructions, in: R. Aguilar, D. Torrealva, S. Moreira, M.A. Pando, L.F. Ramos (Eds.), Structural Analysis of Historical Constructions, Springer International Publishing, Cham, 2019, pp. 429–436.

[39] S. Peña-Villasenín, M. Gil-Docampo, J. Ortiz-Sanz, 3-D modeling of historic façades using SFM photogrammetry metric documentation of different building types of a historic center, Int. J. Archit. Heritage 11 (2017) 871–890, https://doi.org/10.1080/15583058.2017.1317884.

[40] K.O. Al, Structure from motion (SfM) photogrammetry as alternative to laser scanning for 3D modelling of historical monuments, Open Sci. J. 5 (1–17) (2020), https://doi.org/10.23954/osj.v5i2.2327.

[41] C. Briceño, S. Moreira, M.F. Noel, M. Gonzales, E. Vila-Chã, R. Aguilar, Seismic vulnerability assessment of a 17th century adobe church in the peruvian andes, Int. J. Archit. Heritage 13 (2019) 140–152, https://doi.org/10.1080/15583058.2018.1497224.

[42] L. Truong-Hong, D.F. Laefer, Octree-based, automatic building façade generation from LiDAR data, CAD Computer Aided Design 53 (2014) 46–61, https://doi.org/10.1016/j.cad.2014.03.001.

[43] A.M. D'Altri, G. Milani, S. de Miranda, G. Castellazzi, V. Sarhosis, Stability analysis of leaning historic masonry structures, Autom. Constr. 92 (2018) 199–213, https://doi.org/10.1016/j.autcon.2018.04.003.

[44] G. Castellazzi, A.M.D. Altri, M.S. De, F. Ubertini, An innovative numerical modeling strategy for the structural analysis of historical monumental buildings, Eng. Struct. 132 (2017) 229–248, https://doi.org/10.1016/j.engstruct.2016.11.032.

[45] S.G. Barsanti, G. Guidi. A New Methodology for the Structural Analysis of 3D Digitized Cultural Heritage through FEA. IOP Conf. Ser. Mater. Sci. Eng. 364; 2018. 10.1088/1757-899X/364/1/012005.

[46] N. Kassotakis, V. Sarhosis, B. Riveiro, B. Conde, A.M. D'Altri, J. Mills, et al., Three-dimensional discrete element modelling of rubble masonry structures from dense point clouds, Autom. Constr. 119 (2020) 103365, https://doi.org/10.1016/j.autcon.2020.103365.

[47] B.G. Pantoja-Rosero, R. Achanta, M. Kozinski, P. Fua, F. Perez-Cruz, K. Beyer, Generating LOD3 building models from structure-from-motion and semantic segmentation, Autom. Constr. 141 (2022) 104430, https://doi.org/10.1016/J.AUTCON.2022.104430.

[48] B.G. Pantoja-Rosero, R. Achanta, K. Beyer, Automated image-based generation of finite element models for masonry buildings, Bull. Earthq. Eng. (2023) 1–29, https://doi.org/10.1007/S10518-023-01726-7.
[49] P.B. Lourenço, F. Greco, A. Barontini, M.P. Ciocci, G. Karanikoloudis, Seismic retrofitting project: Modeling of prototype, Buildings (2019).
[50] F. Greco, P.B. Lourenço, Seismic assessment of large historic vernacular adobe buildings in the Andean Region of Peru. Learning from Casa Arones in cusco, J. Build. Eng. 40 (2021) 8–13, https://doi.org/10.1016/j.jobe.2021.102341.
[51] M. Acito, E. Magrinelli, G. Milani, S. Tiberti, Seismic vulnerability of masonry buildings: Numerical insight on damage causes for residential buildings by the 2016 central Italy seismic sequence and evaluation of strengthening techniques, J. Build. Eng. 28 (2020) 101081, https://doi.org/10.1016/j.jobe.2019.101081.
[52] A. Formisano, G. Vaiano, F. Fabbrocino, G. Milani, Seismic vulnerability of Italian masonry churches: The case of the Nativity of Blessed Virgin Mary in Stellata of Bondeno, J. Build. Eng. 20 (2018) 179–200, https://doi.org/10.1016/j.jobe.2018.07.017.
[53] P. Roca, L. Pelà, C. Molins. Selected Papers from the 12th International Conference on Structural Analysis of Historical Constructions (SAHC 2021), International Journal of Architectural Heritage, 17:1, 1-2, doi:10.1080/15583058.2022.2164431.
[54] M. Valente, Earthquake response and damage patterns assessment of two historical masonry churches with bell tower, Eng. Fail. Anal. 151 (2023) 107418, https://doi.org/10.1016/J.ENGFAILANAL.2023.107418.
[55] M. Valente, G. Milani, Damage assessment and partial failure mechanisms activation of historical masonry churches under seismic actions: Three case studies in Mantua, Eng. Fail. Anal. 92 (2018) 495–519, https://doi.org/10.1016/J.ENGFAILANAL.2018.06.017.
[56] A. Franchi, P. Napoli, P. Crespi, N. Giordano, M. Zucca, Unloading and reloading process for the earthquake damage repair of ancient masonry columns: The Case of the Basilica di Collemaggio, Int. J. Archit. Heritage 16 (2022) 1683–1698, https://doi.org/10.1080/15583058.2021.1904056.
[57] M. Prosdocimi, S. Calligaro, G. Sofia, G. Dalla Fontana, P. Tarolli, T. Schenk, et al. Structure from Motion (SfM) Photogrammetry Photogrammetric heritage. Department of Civil and Environmental Engineering and Geodetic Science, The Ohio State University 40;2015:79–95. 10.1002/esp.3767.
[58] L. Piermattei, L. Carturan, A. Guarnieri, Use of terrestrial photogrammetry based on structure-from-motion for mass balance estimation of a small glacier in the Italian alps, Earth Surf. Proc. Land. 40 (2015) 1791–1802, https://doi.org/10.1002/esp.3756.
[59] J.A. Warrick, A.C. Ritchie, G. Adelman, K. Adelman, P.W. Limber, New techniques to measure cliff change from historical oblique aerial photographs and structure-from-motion photogrammetry, J. Coast. Res. 33 (2017) 39–55, https://doi.org/10.2112/JCOASTRES-D-16-00095.1.
[60] Á. Gómez-Gutiérrez, J.J. de Sanjosé-Blasco, J. de Matías-Bejarano, F. Berenguer-Sempere, Comparing two photo-reconstruction methods to produce high density point clouds and DEMs in the Corral del Veleta Rock Glacier (Sierra Nevada, Spain), Remote Sens. (Basel) 6 (2014) 5407–5427, https://doi.org/10.3390/rs6065407.
[61] M.J. Westoby, J. Brasington, N.F. Glasser, M.J. Hambrey, J.M. Reynolds, "Structure-from-Motion" photogrammetry: A low-cost, effective tool for geoscience applications, Geomorphology 179 (2012) 300–314, https://doi.org/10.1016/j.geomorph.2012.08.021.
[62] University of Cantabria. Rehabend 2022 Construction Pathology, Rehabilitation Technology And Heritage Management. 2022.
[63] M.A. Soto Zamora, I.E. Vízcaino Hernández, R.A. Díaz Zeledón, J.J. Velasco González. Application of Digital Close-Range Photogrammetry to the Modeling of Heritage Structural Elements for Its Analysis by FEM 2019;1:342–50. 10.1007/978-3-319-99441-3.
[64] S.P. Bemis, S. Micklethwaite, D. Turner, M.R. James, S. Akciz, T.S. Thiele, et al., Ground-based and UAV-Based photogrammetry: A multi-scale, high-resolution mapping tool for structural geology and paleoseismology, J. Struct. Geol. 69 (2014) 163–178, https://doi.org/10.1016/j.jsg.2014.10.007.
[65] Agisoft, Agisoft metashape user manual, Agisoft Metashape (2020:) 160.
[66] F.I. Apollonio, F. Fantini, S. Garagnani, M. Gaiani, A photogrammetry-based workflow for the accurate 3d construction and visualization of museums assets, Remote Sens. (Basel) 13 (2021) 1–40, https://doi.org/10.3390/rs13030486.
[67] J.-M. Morel, G. Yu, ASIFT: A new framework for fully affine invariant image comparison, SIAM J. Imaging Sci. 2 (2009) 438–469, https://doi.org/10.1137/080732730.
[68] M.A. Fischler, R.C. Bolles, Random sample consensus: A paradigm for model fitting with applications to image analysis and automated cartography, Commun. ACM 24 (1981) 381–395, https://doi.org/10.1145/358669.358692.
[69] Johannes L. Schönberger, Enliang Zheng J-MF& MP. Pixelwise View Selection for Unstructured Multi-View Stereo. European Conference on Computer Vision 2016;16:23–32. 10.1007/978-3-319-46487-9.
[70] B.A. El, Tawantinsuyu en Huaytará, Huancavelica 11 (2003) 41–56.
[71] S.B. Lescano. Desplazamientos hispanos por el Qhapaq Ñan y abandono de asentamientos incas durante el período colonial temprano : el caso de Huaytará 2009:127–31.
[72] J. Pierre, D. Harris. Exploration in the Pisco Valley. 1902.
[73] G. Gasparini, L. Margollies. Inca architecture 1980.
[74] D.E. Thompson, G. Gasparini, L. Margolies, P.J. Lyon. Inca Architecture. vol. 17. 1982. 10.2307/2801755.
[75] Imprenta_Americana. Anuario de la Legislacion Peruana 1925. vol. Tomo XX. 1926.
[76] Seiner LIzárraga L. Historia de los sismos en el Perú. Catálogo: Siglos XV-XVII. Lima: 2009.
[77] E. Cuadros-Rojas, L. Pelà, S. Saloustros, N. Tarque, Análisis estructural avanzado del Templo de Huaytará-Huancavelica, Perú (2020).
[78] European Committee for Standardization (CEN). EN 772-1:2011+A1:2016 Methods of test for masonry units – Part 1: Determination of compressive strength (2016).
[79] Ministerio de Transportes y Comunicaciones. Lima Peru. NTP E.070 "Norma Técnica de Albañilería." (2006).
[80] Ministerio de Transportes y Comunicaciones. Lima Peru. NTP E.080 "Norma de diseño y construcción con tierra reforzada." (2017).
[81] European Committee for Standardization (CEN). EN 1926:2007 Natural stone test methods - Determination of uniaxial compressive strength (2007).
[82] European Committee for Standardization (CEN). EN 14580:2006 Natural stone test methods - Determination of static elastic modulus (2006).
[83] DIN. DIN 18555-9:1999 Testing of mortars containing mineral binders – Part 9: Hardened mortars. Determination of the mortar compressive strength in the bed joint (1999).
[84] American Society for Testing and Material (ASTM). ASTM D 7012-14e1 Standard Test Methods for Compressive Strength and Elastic Moduli of Intact Rock Core Specimens under Varying States of Stress and Temperatures (2015);7:37–72.
[85] L. Pelà, P. Roca, A. Aprile, Combined in-situ and laboratory minor destructive testing of historical mortars, Int. J. Archit. Heritage 12 (2018) 334–349, https://doi.org/10.1080/15583058.2017.1323247.
[86] TNO, DIsplacement method ANAlyser (DIANA FEA), release 10.2, Delft, Netherlands, 2018.
[87] M. Núñez García, S. Saloustros, F. Mateos Redondo, J.A. Alonso Campanero, J. Ortega, F. Greco, et al. Seismic Retrofit of Existing Structures Based on Digital Surveying, Non-Destructive Testing and Nonlinear Structural Analysis: The Case of Gjirokastra Castle in Albania. Appl. Sci. 12;2022:12106. doi:10.3390/APP122312106.
[88] G. Karanikoloudis, P.B. Lourenço, Structural assessment and seismic vulnerability of earthen historic structures. Application of sophisticated numerical and simple analytical models, Eng. Struct. 160 (2018) 488–509, https://doi.org/10.1016/J.ENGSTRUCT.2017.12.023.
[89] B.G. Pantoja-Rosero, R. Achanta, K. Beyer, Damage-augmented digital twins towards the automated inspection of buildings, Autom. Constr. 150 (2023) 104842, https://doi.org/10.1016/J.AUTCON.2023.104842.
[90] M. Angelillo, P.B. Lourenço, Masonry behaviour and modelling, Mechanics of masonry structures 551 (2014), https://doi.org/10.1007/978-3-7091-1774-3.
[91] P. Lourenço, Recent advances in masonry modelling: micromodelling and homogenisation, Multiscale Modeling in Solid Mechanics Computational Approaches (2009) 251–294.
[92] P.B. Lourenço, J. Pereira. Recommendations for Advanced Modeling of Historic Earthen Sites. 2018.
[93] M.F. Noel, S. Moreira, C. Briceño, E. López-Hurtado, R. Aguilar, Seismic Assessment of the Church of San Sebastian in Cusco, Peru by Means of Pushover Nonlinear Analysis, in: R. Aguilar, D. Torrealva, S. Moreira, M.A. Pando, L.F. Ramos (Eds.), Structural Analysis of Historical Constructions – an Interdisciplinary Approach, vol. 18, Springer International Publishing, Cusco, Peru, 2019, pp. 1949–1958, https://doi.org/10.1007/978-3-319-99441-3.

[94] S. Tezcan, N. Tambe, C. Muir, R. Aguilar, R. Perucchio. Nonlinear FE Analysis of the Response to Lateral Accelerations of the Triumphal Arch of the Church of Andahuaylillas, Peru Selman. vol. 18. Springer International Publishing; 2019. doi:10.1007/978-3-319-99441-3.
[95] N. Tarque, G. Camata, E. Spacone, H. Varum, M. Blondet, Nonlinear dynamic analysis of a full-scale unreinforced adobe model, Earthq. Spectra 30 (2012) 1643–1661, https://doi.org/10.1193/022512EQS053M.
[96] N. Tarque, G. Camata, H. Varum, E. Spacone, M. Blondet, Numerical simulation of an adobe wall under in-plane loading, Earthq. Struct. 6 (2014) 627, https://doi.org/10.12989/eas.2014.6.6.627.
[97] EN 1996-1-1:2005. Eurocode 6: Design of masonry structures – Part 1-1: General rules for buildings – rules for reinforced and unreinforced masonry 2005.
[98] American Society of Civil Engineers. ASCE 41-06: Seismic Rehabilitation of Existing Buildings 2007:488.
[99] Circolare. Instruction for the application of the building code for constructions (Istruzioni per l'applicazione dell'«Aggiornamento delle "Norme tecniche per le costruzioni"» di cui al decreto ministeriale 17 gennaio 2018) 2019.
[100] MIT 2019. Circolare del ministero delle infrastructure e dei trasporti, n.7 del 21 Gennaio 2019: "Istruzioni per l'applicazione dell'aggiornamento delle Norme tecniche per le costruzioni di cui al D.M. 17 gennaio 2018. Consiglio Superiore Dei Lavori Pubblici GU n35 Del 11022019 2019.
[101] L. Lipa, N. Tarque, L. Pelà, J.M. Goicolea, Evaluation of the seismic behaviour of an inca stone wall using rigid body dynamic methods, RILEM Bookseries 47 (2024) 1102–1113, https://doi.org/10.1007/978-3-031-39603-8_88.
[102] P. Ita, S. Santa-Cruz, D. Daudon, N. Tarque, A. Párraga, V. Ramos, Out-of-plane analysis of dry-stone walls using a pseudo-static experimental and numerical approach in natural-scale specimens, Eng. Struct. 288 (2023) 116153, https://doi.org/10.1016/J.ENGSTRUCT.2023.116153.
[103] G. Vasconcelos. Experimental investigations on the mechanics of stone masonry: Characterization of granites and behavior of ancient masonry shear walls. Universidade do Minho, 2003.
[104] OPCM 3431. Primi elementi in materia di criteri generali per la classificazione sismica del territorio nazionale e di normative tecniche per le costruzioni in zona sismica. Ordinanza del Presidente del Consiglio dei ministri (OPCM), Italy, March 20, 2003, no. 3274, 2005.
[105] EN 1992-1-1:2004. Eurocode 2: Design of concrete structures – Part 1: General rules and rules for buildings 2004.
[106] F. Peter, A nonlinear analysis method for performance-based seismic design, Earthq. Spectra 16 (2000) 573–592.
[107] Standard E. Eurocode 8: Design of structures for earthquake resistance 2001.
[108] S. Lagomarsino, S. Cattari, PERPETUATE guidelines for seismic performance-based assessment of cultural heritage masonry structures, Bull. Earthq. Eng. 13 (2015) 13–47, https://doi.org/10.1007/S10518-014-9674-1.
[109] M.V. Requena-Garcia-Cruz, E. Romero-Sánchez, M.P. López-Piña, A. Morales-Esteban, Preliminary structural and seismic performance assessment of the Mosque-Cathedral of Cordoba: The Abd al-Rahman I sector, Eng. Struct. 291 (2023) 116465, https://doi.org/10.1016/J.ENGSTRUCT.2023.116465.
[110] D. Faiella, M. Argenziano, F. Esposito, G. Brandonisio, M. Fraldi, E. Mele, Effectiveness of isolated vertical extension of masonry buildings as nonconventional TMD, Soil Dyn. Earthq. Eng. 165 (2023) 107675, https://doi.org/10.1016/J.SOILDYN.2022.107675.
[111] F.S. Liguori, S. Fiore, F.L. Perelli, D. De Gregorio, G. Zuccaro, A. Madeo, A mechanical-based seismic vulnerability assessment method with an application to masonry structures in Cosenza (Italy), Bull. Earthq. Eng. 21 (2023) 5655–5681, https://doi.org/10.1007/S10518-023-01752-5.
[112] K. Ožić, I. Markić, A. Moretić, The Assessment and Retrofitting of Cultural Heritage—A Case Study of a Residential Building in Glina, Buildings 13 (2023) 1798, https://doi.org/10.3390/buildings13071798.
[113] A.H. Lazizi, H. Tahghighi, Influence of soil–structure interaction on seismic demands of historic masonry structure of Kashan Grand Bazaar, Bull. Earthq. Eng. 21 (2023) 151–176, https://doi.org/10.1007/s10518-022-01549-y.
[114] A. D'Ambrisi, V. Mariani, M. Mezzi, Seismic assessment of a historical masonry tower with nonlinear static and dynamic analyses tuned on ambient vibration tests, Eng. Struct. 36 (2012) 210–219, https://doi.org/10.1016/J.ENGSTRUCT.2011.12.009.
[115] Ministerio de Vivienda Construcción y Saneamiento. Norma Técnica de Edificación E.030 Diseño Sismorresistente. El Peruano 2019.